Supporting Information

Chemistry of Herz Radicals: A New Way to Near-IR Dyes with Multiple Long-Lived and Differently-Colored Redox States†

Alexander Yu. Makarov,[a] Yulia M. Volkova,[a] Leonid A. Shundrin,*[,a,b] Alexey A. Dmitriev,[c,d] Irina G. Irtegova,[a] Irina Yu. Bagryanskaya,[a,b] Inna K. Shundrina,[a] Nina P. Gritsan,[c,d,*] Jens Beckmann,*[,e] and Andrey V. Zibarev*[,a,f]

a Institute of Organic Chemistry, Russian Academy of Sciences, 630090 Novosibirsk, Russia
E-mail: zibarev@nioch.nsc.ru
E-mail: shundrin@nioch.nsc.ru

b Department of Natural Sciences, Novosibirsk State University, 630090 Novosibirsk, Russia

c Institute of Chemical Kinetics and Combustion, Russian Academy of Sciences, 630090 Novosibirsk, Russia
E-mail: gritsan@kinetics.nsc.ru

d Department of Physics, Novosibirsk State University, 630090 Novosibirsk, Russia

e Institute for Inorganic Chemistry and Crystallography, University of Bremen, 28359 Bremen, Germany
E-mail: j.beckmann@uni-bremen.de

f Department of Chemistry, Tomsk State University, 634050 Tomsk, Russia

† Dedicated to the memory of Prof. Dr. Rüdiger Mews (02.10.1942–04.04.2019)

Contents

8. Electron paramagnetic resonance spectroscopy

9. Spectroelectrochemistry

10. References

1. ORCID identification numbers

0000-0001-9642-8105 (A. Yu. Makarov)

0000-0002-0692-6838 (Yu. M. Volkova)

0000-0002-5091-2812 (L. A. Shundrin)

0000-0001-6260-8124 (A. A. Dmitriev)

0000-0001-7218-6690 (I. G. Irtegova)

0000-0001-7760-5540 (I. Yu. Bagryanskaya)

0000-0002-5091-2812 (I. K. Shundrina)

0000-0002-2263-1300 (N. P. Gritsan)

0000-0002-8548-1821 (J. Beckmann)

0000-0002-5961-423X (A. V. Zibarev)

2. Syntheses

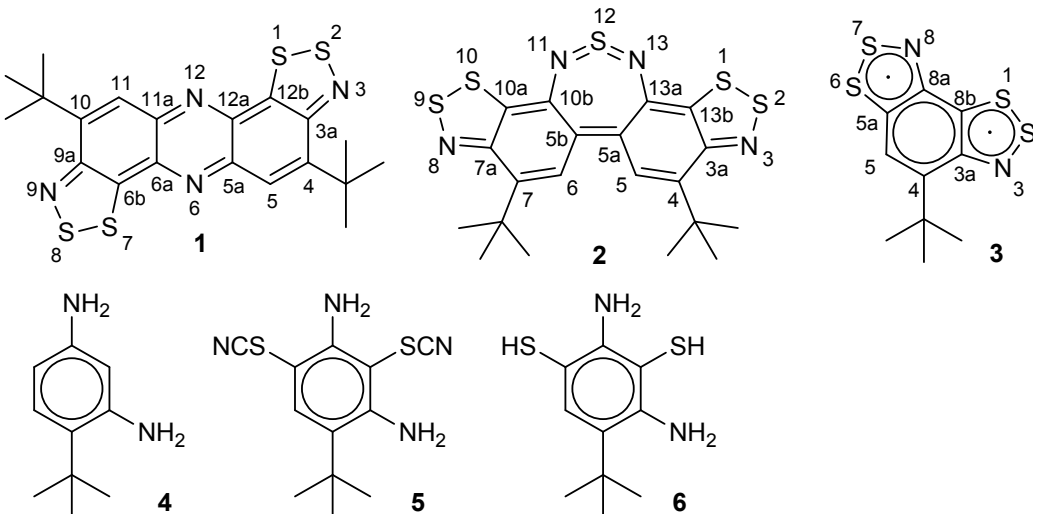

Scheme S1. Numbering of compounds and their atoms.

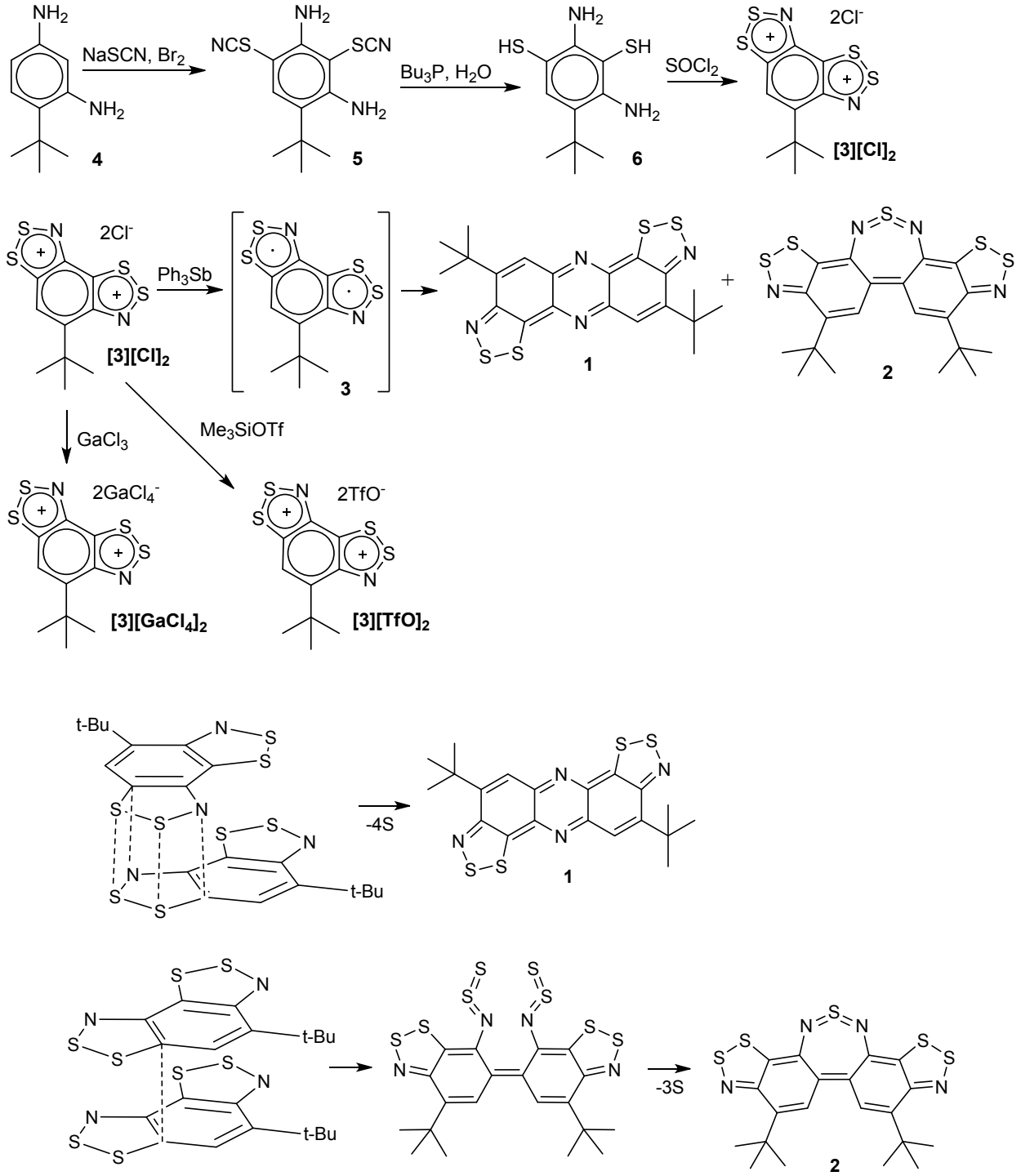

Scheme S2. Synthetic pathways (TfO = CF_3SO_3).

2.1. General

^{1}H NMR spectra were measured in $CDCl_3$ (unless otherwise indicated) with a Bruker AV-400 spectrometer at frequency of 400.1 MHz with TMS as a standard. MS spectra were taken with Thermo Electron DFS machine. UV-Vis spectra were collected with Varian Cary 5000 spectrophotometer. Simultaneous thermogravimetry and differential scanning calorimetry

measurements were performed with a Netzsch STA 409 instrument. IR spectra were obtained in KBr pillets with Vector 22 instrument.

Elemental analysis was performed with Carlo Erba Model 1106 device, as well as by means of traditional combustion. With both techniques, data on C for compound **2** were only satisfactory for unclear reasons in front of correct analyses on other elements. Similar problems were observed with salts [**1**][Cl]$_2$, [**1**][$GaCl_4$] · ½C_6H_{14}, [**3**][$GaCl_4$]$_2$ · Et_2O and [**3**][CF_3SO_3]$_2$ – most likely due to enormous instability of their cations towards traces of moisture, together with loss of solvate molecules in the cases of [**1**][$GaCl_4$] · ½C_6H_{14} and [**3**][$GaCl_4$]$_2$ · Et_2O during storage and handling. Salt [**3**][Cl]$_2$ was used as a crude product without additional purification. For salt [**1**][$GaCl_4$] unambiguously characterized by XRD and EPR, satisfactory elemental analysis data were not obtained – most likely due to the aforementioned instability of cation towards traces of moisture.

Starting 1-*tert*-butyl-2,4-diaminobenzene **4** was synthesized by known methods.[1]

2.2. Synthetic protocols

1-Tert-butyl-2,4-diaminobenzene-3,5-bis(thiocyanate) 5. A solution of Br_2 (1.38 mL, 4.30 g, 27 mmol) in MeOH (10 mL) was added over 15 min to a stirred mixture of compound **4** (2.00 g, 12.2 mmol), NaSCN·2H_2O (4.28 g, 36.6 mmol) and EtOH (30 mL) at –30 °C. After 30 min at ambient temperature, the mixture was poured into water (150 mL), dark precipitate was filtered off, washed with water, dried and washed with Et_2O. The solid was dissolved in CH_2Cl_2, the solution was filtered and concentrated. The precipitate of compound **5** was filtered off, washed with small amount of CH_2Cl_2 and dried. The mother liquor was flash chromatographed with short silica column and eluate concentrated to give additional precipitate of the product. Compound **5** was obtained in the form of white powder, 2.10 g (62%), m. p. 192-195 °C. ^{1}H NMR, δ: 7.39 (s, 1H), 5.13 (s, 2H), 5.09 (s, 2H), 1.37 (s, 9H). MS, m/z, measured (calculated for $C_{12}H_{14}N_4S_2$): 278.0656 (278.0654). IR (ν, cm^{-1}): 3498 m, 3475 s, 2970 m, 2875 w, 2152 s, 1612 vs, 1529 m, 1468 s, 1416 m, 1398 m, 1371 w, 1294 m, 1244 m, 756 w, 476 w. Found (%): C 51.30; H 5.03; N 19.79; S 23.06. Calculated for $C_{12}H_{14}N_4S_2$ (%): C 51.77; H 5.09; N 20.12; S 23.04.

4-Tert-butylbenzo[1,2-d:3,4-d']bis([1,2,3]dithiazolium) dichloride [3][Cl]$_2$. Under argon, a solution of Bu_3P (1.1 mL, 4.4 mmol) in Et_2O (5 mL) was added to a mixture of compound **5** (0.56 g, 2 mmol), H_2O (0.1 mL, 5.5 mmol) and Et_2O (10 mL). The clear solution was formed in 10 min. After 30 min, a solution prepared from Et_2O (5 mL), EtOH (0.3 mL) and Me_3SiCl (0.65

mL) was added to the reaction mixture. The emulsion formed was stirred until appearance of the solid precipitate. The solution was decanted and the precipitate was washed by Et_2O (3 × 10 mL). Then $SOCl_2$ (20 mL) was added and the reaction refluxed for 30 min. The precipitate was filtered off, washed with $SOCl_2$ and dried under vacuum. Compound [**3**][Cl]$_2$ was obtained in the form of dark-red powder, 0.38 g (53%), m. p. >360 °C. ^{1}H NMR (CF_3CO_2H / $CDCl_3$ 3 : 1), δ: 9.44 (br. s), 1.85 (br. s) (signal broadening caused minor admixture of the radical cation of compound **3** detected by EPR, see below). Found (%): C 31.49; H 3.05; Cl 22.00; N 8.42; S 32.60. Calculated for $C_{10}H_{10}Cl_2N_2S_4$ (%): C 33.61; H 2.82; Cl 19.84; N 7.84; S 35.89. This crude product was used in the following preparations without further purification.

4-Tert-butylbenzo[1,2-d:3,4-d']bis([1,2,3]dithiazolium) bis(tetrachlorogallate), solvate with diethyl ether, [3][$GaCl_4$]$_2$ · Et_2O. A solution of $GaCl_3$ (0.26 g, 1.46 mmol) in MeCN (0.8 mL) was added to compound [**3**][Cl]$_2$ (0.26 g, 0.73 mmol). The reaction mixture was periodically shaken. After 6 h, the solution was evaporated in vacuo and Et_2O (5 mL) was added to the residue. After 16 h the solvent was removed with syringe, the crystalline residue was washed with Et_2O and dried in vacuo. Compound [**3**][$GaCl_4$]$_2$ · Et_2O was obtained in the form of yellow crystals suitable for XRD, 0.51 g (88%), dec. 130-160 °C. ^{1}H NMR (CD_3CN), δ: 9.19 (br. s, 1H), 3.42 (q, 4H), 1.77 (s, 9H), 1.11 (t, 6H). Found: C 20.66; H 2.28; Cl 35.05; N 3.50; S 16.37. Calculated for $C_{14}H_{20}Cl_8Ga_2N_2OS_4$ (%): C 21.46; H 2.57; Cl 36.19; N 3.57; S 16.37.

4-Tert-butylbenzo[1,2-d:3,4-d']bis([1,2,3]dithiazolium) bis(trifluoromethanesulfonate) [3][CF_3SO_3]$_2$. Under argon, $CF_3SO_2OSiMe_3$ (0.2 mL, 1.1 mmol) was added to a stirred suspension of compound [**3**][Cl]$_2$ (0.15 g, 0.41 mmol) in MeCN (5 mL). After 3.5 h, the green-yellow precipitate was filtered off, subsequently washed with MeCN (2 mL) and Et_2O (5 mL), and dried under argon stream. Compound [**3**][CF_3SO_3]$_2$ was obtained in the form of greenish-yellow powder, 0.10 g (40%), m. p. 278-280 °C (dec.). UV-Vis (CF_3CO_2H). λ_{max}, nm, (log ε): 342 (4.52), 398 (3.92). Found (%): C 25.27; H 1.65; F 19.07; N 4.98; S 29.85. Calculated for $C_{12}H_{10}F_6N_2O_6S_6$ (%): C 24.65; H 1.72; F 19.50; N 4.79; S 32.91. Crystals suitable for XRD were obtained by slow diffusion in MeCN / Et_2O two-layered system.

4,10-Di-tert-butylbis([1,2,3]dithiazolo)[5,4-a:5',4'-h]phenazine 1 and 4,7-di-tert-butylbis[1,2,3]dithiazolo[4'5':3,4;5',4':8,9]dibenzo[c,e][1λ^{4}δ^2,2,7]thiadiazepine 2. Ph_3Sb (0.353 g, 1 mmol) was added to a refluxed suspension of compound [**3**][Cl]$_2$ (0.357 g, 1 mmol) in MeCN (10 mL). After 1 h, the reaction mixture was cooled to room temperature, and the precipitate was filtered off, washed with MeCN and chromatographed on silica column with

CH_2Cl_2 containing 1 vol. % of NEt_3. For the purple-blue-green zone, the eluate was collected and evaporated, and crude mixture of compounds **1** and **2** was washed with 1 : 1 : 1 mixture of hexane, CH_2Cl_2 and CCl_4 until the procedure gave green solution. The solid remained was compound **1**.

The solution was chromatographed on silica column with 1 : 1 : 1 mixture of hexane, CH_2Cl_2 and CCl_4 containing 1 vol. % of NEt_3. For the blue-purple zone, the eluate was collected and evaporated, the admixtures of sulfur and Ph_3Sb were sublimed at 90 ^oC / 0.5 Torr and the residue recrystallized from CCl_4 which gave compound **2**. For the green zone, the eluate was collected, evaporated, and the residue combined with the previous sample of compound **1** was recrystallized from CCl_4.

Compound **1** (Figure S1) was obtained in the form of lustrous red-purple crystals suitable for XRD, 93.8 mg (42%), m. p. 325 ^oC (dec.). ^1H NMR, δ: 7.34 (s, 2H), 1.47 (s, 18H). MS, m/z, measured (calculated for $C_{20}H_{20}N_4S_4$): 444.0563 (444.0564). UV-Vis ($CHCl_3$), λ_{max}, nm, (log ε): 317 (4.35), 334 (4.29), 354 (4.26), 408 (3.47), 433 (3.66), 464 (3.70), 517 (3.23), 689 (4.72). Found (%): C 54.39; H 4.51; N 12.53; S 28.72. Calculated for $C_{20}H_{20}N_4S_4$ (%): C 54.02; H 4.53; N 12.60; S 28.84.

Compound **2** (Figure S1) was obtained in the form of black crystals with green luster, 20.4 mg (8.6%), m. p. 270 ^oC (dec.). ^1H NMR, δ: 7.18 (s, 2H), 1.36 (s, 18H). MS, m/z, measured (calculated for $C_{20}H_{20}N_4S_5$): 476.0289 (476.0286). UV-Vis ($CHCl_3$), λ_{max}, nm, (log ε): 240 (4.17), 319 (4.09), 367 (4.12), 562 (4.54), 599 (4.49), 744 (4.11), 796 (4.08). Found (%): C 49.67; H 4.17; N 11.42; S 33.39. Calculated for $C_{20}H_{20}N_4S_5$ (%): C 50.39; H 4.23; N 11.75; S 33.63. Crystals of **2** suitable for XRD were obtained by slow evaporation of its solution in $CHCl_3$.

Figure S1. Compounds **1** and **2** in the solid state and THF solution.

Reduction of compound [**3**][Cl]$_2$ with Ph_3Sb at ambient temperature gave compounds **1** and **2** in yields 9 and 4%, respectively. Reduction by Me_3SiN_3 (2-fold excess in MeCN at reflux) gave only compound **1** in 14% yield.

4,10-Di-tert-butylbis([1,2,3]dithiazolo)[5,4-a:5',4'-h]phenazine-2,8-diium dichloride [1][Cl]$_2$. 4-$CH_3C_6H_4ICl_2$ (16 mg, 5.5×10^{-5} mol) was added to a stirred suspension of compound **1** (22 mg, 5×10^{-5} mol) in CH_2Cl_2 (2.5 mL). After 30 min, the red-brown precipitate was filtered off, washed with CH_2Cl_2 and dried under vacuum. Compound [**1**][Cl]$_2$ was obtained in the form of brown powder, 25.3 mg (98%), m. p. > 360 ^{o}C. ^{1}H NMR (CF_3CO_2H / $CDCl_3$ 3:1): 8.72 (s, 2H), 1.81 (s, 18H). UV-Vis (CF_3CO_2H), λ_{max}, nm, (log ε): 347 (4.71), 407 (4.42). Found (%): C 44.56; H 3.65; N 10.26; S 23.42; Cl 15.16. Calculated for $C_{20}H_{20}Cl_2N_4S_4$ (%): C 46.59; H 3.91; N 10.87; S 24.88; Cl 13.75. This crude product was used further without purification.

4,10-Di-tert-butylbis([1,2,3]dithiazolo)[5,4-a:5',4'-h]phenazine-2,8-diium bis(trifluoromethanesulfonate) [1][CF_3SO_3]$_2$ and its solvate with acetonitrile. Under argon, $CF_3SO_3SiMe_3$ (0.02 mL, 1.1×10^{-4} mol) was added to a stirred suspension of [**1**][Cl]$_2$ (25.7 mg, 5×10^{-5} mol) in MeCN (6 mL). After 3.5 h, the red-purple precipitate was filtered off, washed with Et_2O (20 mL), and dried under vacuum. Compound [**1**][CF_3SO_3]$_2$ was obtained in the form

of red-purple powder, 27.2 mg (63%), m. p. > 360 °C. UV-Vis (CF_3CO_2H). λ_{max}, nm, (log ε): 347 (4.70), 408 (4.46). Found (%): C 34.86; H 2.58; F 15.14; N 7.43; S 24.25. Calculated for $C_{22}H_{20}F_6N_4O_6S_6$ (%): C 35.57; H 2.71; F 15.35; N 7.54; S 25.90. Crystals suitable for XRD were obtained by recrystallization from MeCN as [**1**][CF_3SO_3]$_2$ · 2MeCN.

4,10-Di-tert-butylbis([1,2,3]dithiazolo)[5,4-a:5',4'-h]phenazine-2,8-diium bis(tetrachlorogallate), solvates with toluene and acetonitrile, [1][$GaCl_4$]$_2$ · 2$CH_3C_6H_5$ and [1][$GaCl_4$]$_2$ · 2MeCN. A solution of $GaCl_3$ (17.6 mg, 1×10^{-4} mol) in MeCN (0.1 mL) was added to a suspension of compound [**1**][Cl]$_2$ (23.6 mg, 4.5×10^{-5} mol) in MeCN (1 mL). After 30 min, toluene (7 mL) or Et_2O (20 mL, in the way forming two-layered system) were added. After 2 days at 0 °C, the crystalline precipitate was filtered off, washed with toluene or Et_2O, and dried under vacuum.

Compound [**1**][$GaCl_4$]$_2$ · 2$CH_3C_6H_5$ was obtained in the form of dark brown needles suitable for XRD, 37 mg (85%), m. p. 295-300 °C (dec.; toluene losing at 106 °C). ^{1}H NMR (CD_3CN), δ: 8.68 (s, 2H), 7.22 (t, 4H), 7.16 (d, 4H), 7.12 (t, 2H), 2.31 (s, 6H), 1.79 (s, 18H). Found (%): C 38.64; H 3.45; Cl 27.11; N 5.33; S 11.97. Calculated for $C_{34}H_{36}Cl_8Ga_2N_4S_4$ (%): C 38.82; H 3.38; Cl 26.96; N 5.24; S 12.19.

Compound [**1**][$GaCl_4$]$_2$ · 2MeCN was obtained in the form of dark brown needles suitable for XRD, 36.5 mg (76%), m. p. 298-300 °C (dec.; acetonitrile losing at 105-110 °C). Found (%): C 30.25; H 2.75; Cl 29.89; N 8.85; S 13.60. Calculated for $C_{24}H_{26}Cl_8Ga_2N_6S_4$ (%): C 30.35; H 2.76; Cl 29.86; N 8.85; S 13.50.

4,10-Di-tert-butylbis([1,2,3]dithiazolo)[5,4-a:5',4'-h]phenazinylium tetrachlorogallate [1][$GaCl_4$]. A mixture of compounds **1** (7.9 mg, 1.8×10^{-5} mol) and [**1**][$GaCl_4$]$_2$ · 2$CH_3C_6H_5$ (18.6 mg, 1.8×10^{-5} mol) with MeCN (10 mL) was stirred for 4 h, filtered and evaporated in vacuo. The residue was washed with toluene, dried in vacuo and dissolved in MeCN (2 mL) under reflux. The solution was cooled to ambient temperature and Et_2O (30 mL) was added to form two-layered system. The system was kept at 0 °C until mutual diffusion of solvents ceased. The precipitate was filtered off, washed with Et_2O and dried in vacuo. Compound [**1**][$GaCl_4$] was obtained in the form of dark brown crystals suitable for XRD, 8 mg (34%), m. p. > 360 °C.

4,10-Di-tert-butylbis([1,2,3]dithiazolo)[5,4-a:5',4'-h]phenazinylium tetrachlorogallate, solvate with hexane, [1][$GaCl_4$] · ½C_6H_{14}. A mixture of compounds **1** (10.1 mg, 2.3×10^{-5} mol) and [**1**][$GaCl_4$]$_2$ · 2$CH_3C_6H_5$ (24.0 mg, 2.3×10^{-5} mol) with THF (9 mL) was stirred for 4 h, filtered. Then hexane (20 mL) was added to form two-layered system. After mutual diffusion

ceased, the precipitate was filtered off, washed with hexane and dried in vacuo. Compound [**1**][$GaCl_4$] · ½C_6H_{14} was obtained in the form of black fibrous crystals, 25.4 mg (76%), m. p. > 360 °C. Found (%): C 39.57; H 3.88; Cl 18.20; N 8.00; S 18.34. Calculated for $C_{23}H_{27}Cl_4GaN_4S_4$ (%): C 39.50; H 3.89; Cl 20.28; N 8.01; S 18.34.

3. X-ray diffraction

XRD measurements (Figures 1 and 6 of the main text; Figure S2, Table S1) were performed with a Bruker Kappa Apex II CCD diffractometer using φ,ω-scans of narrow (0.5°) frames with Mo Kα radiation (λ = 0.71073 Å) and a graphite monochromator. The structures were solved by direct methods using the *SHELX-97* program[2] and refined by full-matrix least-squares method against all F^2 in anisotropic approximation using the *SHELXL-2014/7* program.[3] The hydrogen atoms positions were calculated with the riding model. Absorption corrections were applied using the empirical multiscan method with the *SADABS* program.[4]

In [**1**]$^{\bullet+}$[$GaCl_4$]$^-$, the Ga atom is disordered over two positions with three Cl atoms being common for them, whereas the fourth Cl atom is disordered over the two positions.

With the *PLATON*[5] routine analysis, free solvent accessible volumes in the unit cells of compounds **2** and [**1**]$^{2+}$[$GaCl_4$]$^-_2$ · 2$CH_3C_6H_5$ were estimated as 172.0 Å^3 (14.6% of the unit cell volume) and 355.0 Å^3 (31.9% of the unit cell volume), respectively. These volumes are occupied by heavily disordered solvate molecules, $CHCl_3$ and $CH_3C_6H_5$, respectively, which could not be modeled by sets of discrete atomic sites. With the *PLATON SQUEEZE* procedure, the contributions to the diffraction from the solvate regions were calculated to obtain sets of solvent-free diffraction intensities. For [**1**]$^{2+}$[$GaCl_4$]$^-_2$ · 2$CH_3C_6H_5$ difference electron density synthesis with coefficients Fo-Fc revealed two solvate molecules in asymmetric unit (their presence was also confirmed by elemental analysis and ^{1}H NMR data). However, for the solvate molecules H atoms of CH_3 group were not localized due to strong disorder. The obtained crystal structures were analyzed for shortened contacts between non-bonded atoms using the *PLATON*[5] and *MERCURY* programs.[6]

The supplementary crystallographic data for this paper can be obtained free of charge via http://www.ccdc.cam.ac.uk/cgi-bin/catreq.cgi, or from the Cambridge Crystallographic Data Centre, 12 Union Road, Cambridge CB2 1EZ, UK; fax: (+44) 1223 336 033; or e-mail: deposit@ccdc.cam.ac.uk.

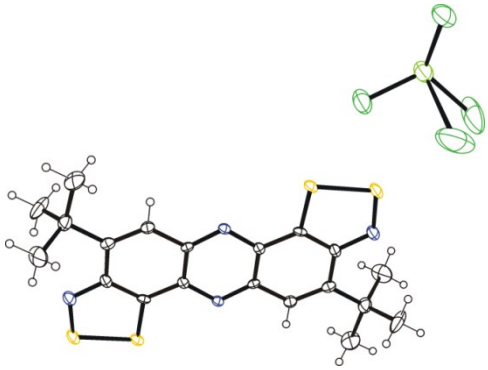

$[\mathbf{1}]^{\bullet+}[GaCl_4]^-$

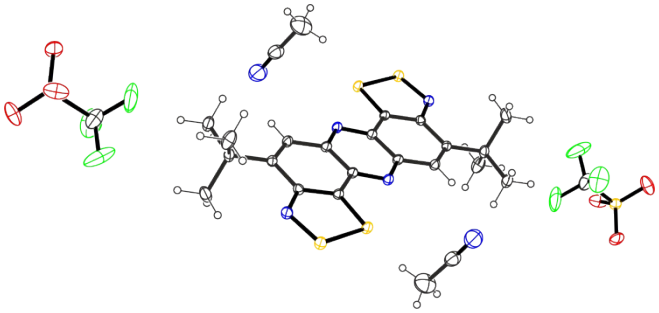

$[\mathbf{1}]^{2+}[CF_3SO_3]^-_2 \cdot 2MeCN$

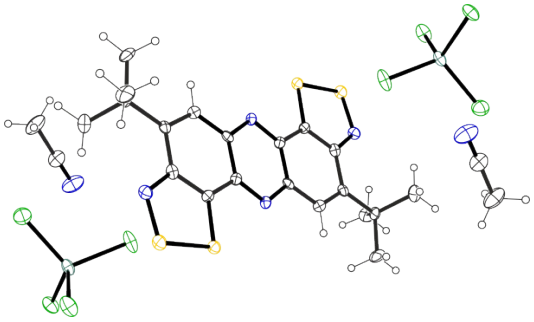

$[\mathbf{1}]^{2+}[GaCl_4]^-_2 \cdot 2MeCN$

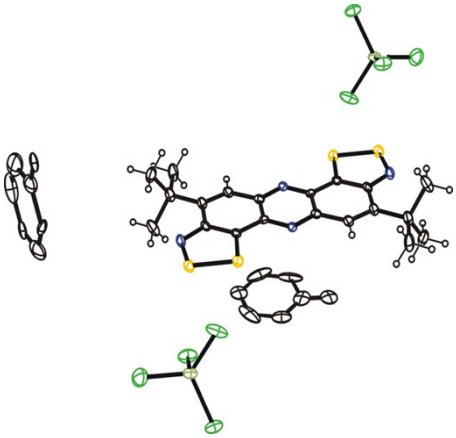

$[\mathbf{1}]^{2+}[GaCl_4]^-_2 \cdot 2CH_3C_6H_5$

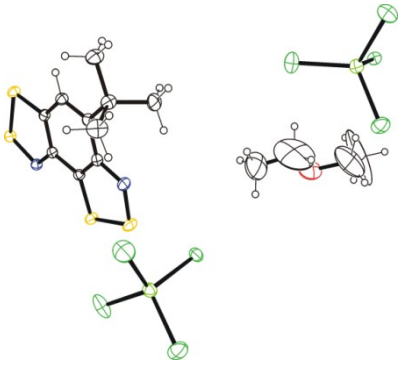

$[\mathbf{3}]^{2+}[GaCl_4]^-_2 \cdot Et_2O$

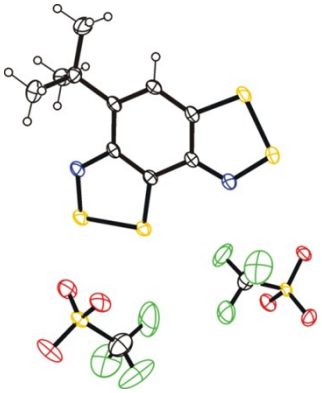

$[\mathbf{3}]^{2+}[CF_3SO_3]^-_2$

Figure S2. XRD structures of compounds (toluene molecules of $[\mathbf{1}]^{2+}[GaCl_4]^-_2 \cdot 2CH_3C_6H_5$ shown without H atoms).

Table S1. Crystallographic data for compounds.[a]

Compound	**1**	**2**	[**1**][$GaCl_4$]
Empirical formula	$C_{20}H_{20}N_4S_4$	$C_{20}H_{20}N_4S_5$	$C_{20}H_{18}N_4S_4$, $GaCl_4$
Formula weight	444.64	476.70	654.14
Temperature K	296(2)	296(2)	296(2)
Wavelength Å	0.71073	0.71073	0.71073
Crystal system	Monoclinic	Monoclinic	Monoclinic
Space group	C2/m	C2/m	I2/m
Unit cell dimensions *a* Å	26.778(5)	26.008(5)	15.6419(11)
b Å	6.838(1)	7.0295(14)	6.7683(5)
c Å	13.634(3)	14.980(3)	25.762(3)
α °	90	90	90
β °	120.56(1)	120.32(3)	100.258(5)
γ °	90	90	90
Volume $Å^3$	2149.8(8)	2364.1(10)	2683.8(4)
Z	4	4	4
Density (calcd.) $Mg.m^{-3}$	1.374	1.339	1.619
Abs. coefficient mm^{-1}	0.456	0.504	1.753
F(000)	928	992	1316
Crystal size mm^3	0.9 × 0.06 × 0.03	0.90 × 0.02 × 0.02	0.90 × 0.04 × 0.02
Θ range for data collection °	2.99–27.54	2.73–27.53	3.11–25.03
Index ranges	$-34 \le h \le 34$, $-7 \le k \le 8$, $-17 \le l \le 17$	$-33 \le h \le 33$, $-9 \le k \le 8$, $-19 \le l \le 19$	$-18 \le h \le 18$, $-8 \le k \le 8$, $-30 \le l \le 30$
Reflections collected	18866	23626	21415
Independent reflections	2670 R(int) = 0.074	2941 R(int) = 0.096	2577 R(int) = 0.057
Completeness to θ %	99.8	99.6	99.4
Data / restraints / parameters	2670 / 8 / 175	2941 / 5 / 201	2577 / 0 / 199
Goodness-of-fit on F^2	1.04	1.05	1.04
Final R indices $I > 2\sigma(I)$	R_1 = 0.0453, wR_2 = 0.1118	R_1 = 0.0479, wR_2 = 0.1114	R_1 = 0.0961, wR_2 = 0.2633
Final R indices (all data)	R_1 = 0.0900, wR_2 = 0.1370	R_1 = 0.0898, wR_2 = 0.1272	R_1 = 0.1219, wR_2 = 0.2951
Largest diff. peak / hole $e.Å^{-3}$	0.39 / –0.36	0.31 / –0.35	1.00 / –1.30
CCDC	**1910727**	**1910728**	**1910729**

Table S1 *(continued)*

Compound	[**1**][$GaCl_4$]$_2$ · 2CH_3CN	[**1**][$GaCl_4$]$_2$ · 2$CH_3C_6H_5$	[**1**][CF_3SO_3]$_2$ · 2CH_3CN
Empirical formula	$C_{20}H_{20}N_4S_4$, 2($GaCl_4$), 2(C_2H_3N)	$C_{20}H_{20}N_4S_4$, 2($GaCl_4$), toluene	$C_{10}H_{10}N_2S_4$, CF_3O_3S, C_2H_3N
Formula weight	949.79	867.68	412.44
Temperature K	200(2)	200(2)	200(2)
Wavelength Å	0.71073	0.71073	0.71073
Crystal system	Orthorhombic	Triclinic	Triclinic
Space group	Pbca	P–1	P–1
Unit cell dimensions *a* Å	17.001(1)	7.196(3)	7.7987(4)
b Å	12.428(1)	10.589(4)	11.1508(6)
c Å	18.431(2)	15.296(7)	11.7044(7)
α °	90	100.190(14)	68.737(2)
β °	90	99.014(15)	82.028(2)
γ °	90	98.771(15)	70.790(2)
Volume Å^3	3894.5(6)	1113.5(8)	895.51(9)
Z	4	1	2
Density (calcd.) Mg.m^{-3}	1.620	1.509	1.530
Abs. coefficient mm^{-1}	2.174	1.905	0.461
F(000)	1896	502	422
Crystal size mm^3	0.35 × 0.30 × 0.15	0.20 × 0.06 × 0.01	0.40 × 0.15 × 0.10
Θ range for data collection °	2.21–25.05	2.76–26.45	2.26–30.07
Index ranges	–20 ≤ h ≤ 20, –14 ≤ k ≤ 14, –21 ≤ l ≤ 21	–8 ≤ h ≤ 8, –13 ≤ k ≤ 13, –19 ≤ l ≤ 19	–10 ≤ h ≤ 10, –15 ≤ k ≤ 15, –15 ≤ l ≤ 16
Reflections collected	38728	18286	15499
Independent reflections	3444 R(int) = 0.088	4447 R(int) = 0.1019	4642 R(int) = 0.026
Completeness to θ %	99.9	99.9	99.5
Data / restraints / parameters	3444 / 0 / 203	4447/ 72 /258	4642 / 0 / 229
Goodness-of-fit on F^2	1.03	1.06	1.01
Final R indices $I > 2\sigma(I)$	R_1 = 0.0584, wR_2 = 0.1489	R_1 = 0.0657, wR_2 = 0.1762	R_1 = 0.0398, wR_2 = 0.1082
Final R indices (all data)	R_1 = 0.0980, wR_2 = 0.1723	R_1 = 0.1249, wR_2 = 0.2072	R_1 = 0.0633, wR_2 = 0.1276
Largest diff. peak / hole e.Å^{-3}	0.66 / –0.50	1.26 / –0.83	0.50 / –0.48
CCDC	**1910731**	**1910733**	**1922816**

Table S1 *(continued)*

Compound	[**3**][$GaCl_4$]$_2$ · $(C_2H_5)_2O$	[**3**][CF_3SO_3]$_2$
Empirical formula	$C_{10}H_{10}N_2S_4$, 2($GaCl_4$), $C_4H_{10}O$	$C_{10}H_{10}N_2S_4$, 2(CF_3O_3S)
Formula weight	783.60	584.58
Temperature K	200(2)	296(2)
Wavelength Å	0.71073	0.71073
Crystal system	Monoclinic	Triclinic
Space group	$P2_1/c$	P–1
Unit cell dimensions *a* Å	12.8899(3)	7.9057(7)
b Å	21.9751(6)	11.866(1)
c Å	10.8024(3)	13.722(1)
α °	90	110.248(4)
β °	98.6730(10)	104.718(4)
γ °	90	97.976(4)
Volume Å^3	3024.86(14)	1131.0(2)
Z	4	2
Density (calcd.) Mg.m^{-3}	1.721	1.717
Abs. coefficient mm^{-1}	2.777	0.686
F(000)	1552	588
Crystal size mm^3	0.60 × 0.40 × 0.08	0.20 × 0.20 × 0.15
Θ range for data collection °	3.20–27.48	2.72–26.13
Index ranges	$-16 \le h \le 16$, $-28 \le k \le 28$, $-14 \le l \le 14$	$-9 \le h \le 9$, $-14 \le k \le 14$, $-16 \le l \le 16$
Reflections collected	45084	19832
Independent reflections	6914 R(int) = 0.026	4485 R(int) = 0.044
Completeness to θ %	99.8	99.3
Data / restraints / parameters	6914 / 5 / 283	4485 / 0 / 292
Goodness-of-fit on F^2	1.07	1.04
Final R indices $I > 2\sigma(I)$	R_1 = 0.0340, wR_2 = 0.0858	R_1 = 0.0458, wR_2 = 0.1093
Final R indices (all data)	R_1 = 0.0490, wR_2 = 0.0939	R_1 = 0.0860, wR_2 = 0.1380
Largest diff. peak / hole e.Å^{-3}	0.86 / –0.73	0.40 / –0.39
CCDC	**1910730**	**1910732**

[a] For [**1**][$GaCl_4$]$_2$ · 2$CH_3C_6H_5$, H atoms of CH_3 group were not localized due to strong disorder.

Molecules of compounds **1** and **2** are planar except groups CH_3. Bond lengths in compounds **1** and **2** are alternated in accordance with their quinoid structures (Scheme S1). In compound **2**, formally double bond C5a–C5b between the carbocycles of 1.437 Å is longer than the carbon-carbon bond in benzene of 1.399 Å. The crystal packing of compounds **1** and **2** (Figure S3) reveals infinite π-stacks with interplanar separation of 3.419 and 3.515 Å, respectively (the sum of van der Waals (VdW) radii of C and S atoms, 3.66 Å).[7]

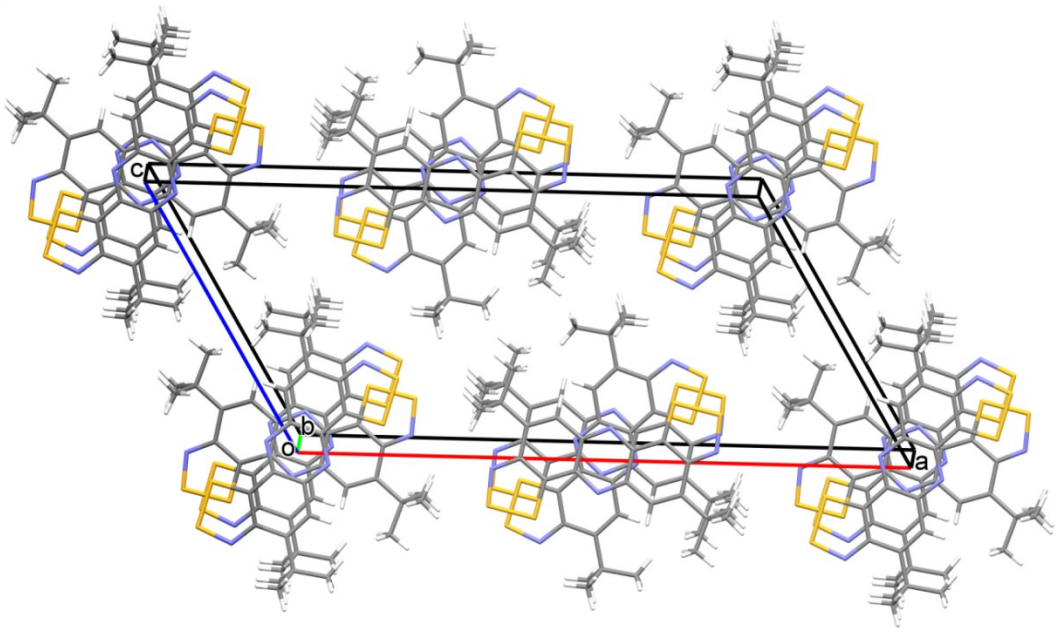

1

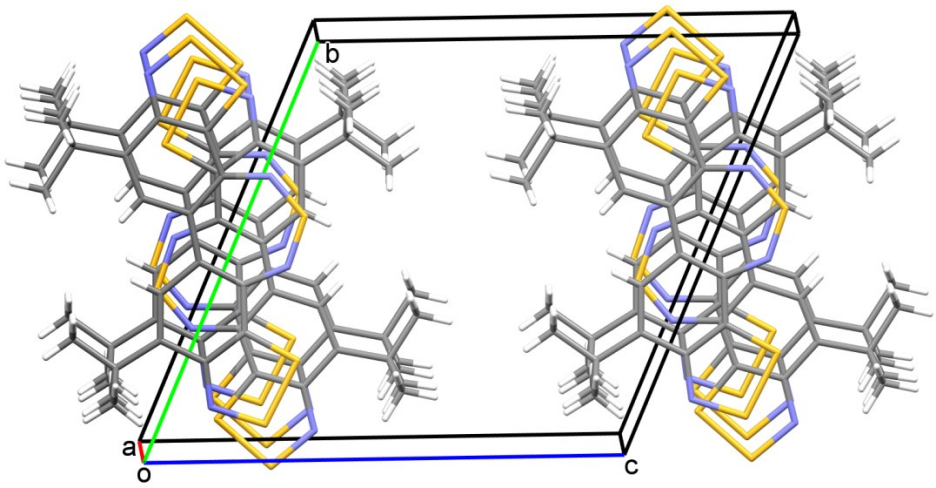

2

Figure S3. Crystal packing of compounds **1** and **2**.

Upon going from **1** to $[\mathbf{1}]^{\bullet+}$, bond distances in the carbocycles remain practically intact, whereas their alternation in the dithiazole cycles gets slightly reduced (Δd_{max} = 0.034 Å). On further going to $[\mathbf{1}]^{2+}$ this bond alternation even more decreases (Δd_{max} = 0.049 Å as compared with $[\mathbf{1}]^{\bullet+}$, and 0.068 Å as compared with **1** (Figures S3-S5, Table S2). Notably, bond distances situation in the other, carbo- and heterocycles of $[\mathbf{1}]^{2+}$ differently depends on solvate molecules (Table S2), which most likely indicates secondary bonding interactions between the species.

Table S2. Selected bond distances in **1**, $[\mathbf{1}]^{\bullet+}$ and $[\mathbf{1}]^{2+}$.[a]

Bond and its formal order[b]	Bond distance (Å) in compound				
	1	$[\mathbf{1}]^{\bullet+}$	$[\mathbf{1}]^{2+}$ [c]	$[\mathbf{1}]^{2+}$ [d]	$[\mathbf{1}]^{2+}$ e
S1–S2 ord.	2.089	2.073	2.027	2.024	2.034
S2–N3 ord.	1.627	1.611	1.588	1.590	1.585
N3–C3a dbl.	1.324	1.332	1.345	1.341	1.336
C3a–C12b ord.	1.425	1.435	1.414	1.426	1.418
C12b–S1 ord.	1.751	1.717	1.684	1.688	1.683
C3a–C4 ord.	1.460	1.452	1.460	1.471	1.460
C4–C5 dbl.	1.351	1.353	1.378	1.340	1.354
C5–C5a ord.	1.444	1.449	1.418	1.459	1.439
C5a–N6, dbl.	1.335	1.323	1.364	1.323	1.339
N12–C12a ord.	1.370	1.380	1.323	1.327	1.336
C5a–C12a ord.	1.430	1.415	1.442	1.423	1.420
C12a–C12b dbl.	1.374	1.386	1.432	1.414	1.431

[a] For atom numbering, see Scheme S1.

[b] Ord. = ordinary, dbl. = double.

[c] $[\mathbf{1}][GaCl_4]^-_2$, solvate with MeCN.

[d] $[\mathbf{1}][GaCl_4]^-_2$, solvate with toluene.

[e] $[\mathbf{1}][TfO]^-_2$, solvate with MeCN.

In the crystal of $[\mathbf{1}]^{\bullet+}[GaCl_4]^-$, there are crystalographically independent 1/2 parts of two radical cations situated at the centers of symmetry, with all atoms except of CH_3 groups lying in the mirror plane. Anion of $[\mathbf{1}]^{\bullet+}[GaCl_4]^-$ is disordered over two sets of positions. The radical cations $[\mathbf{1}]^{\bullet+}$ form infinite π-stacks with interplanar separation of 3.384 Å (Figure S4). In the crystals of $[\mathbf{1}]^{2+}[GaCl_4]^-_2 \cdot 2CH_3C_6H_5$ there are π-stacking interactions between $[\mathbf{1}]^{2+}$ and toluene molecules (Figure S5).

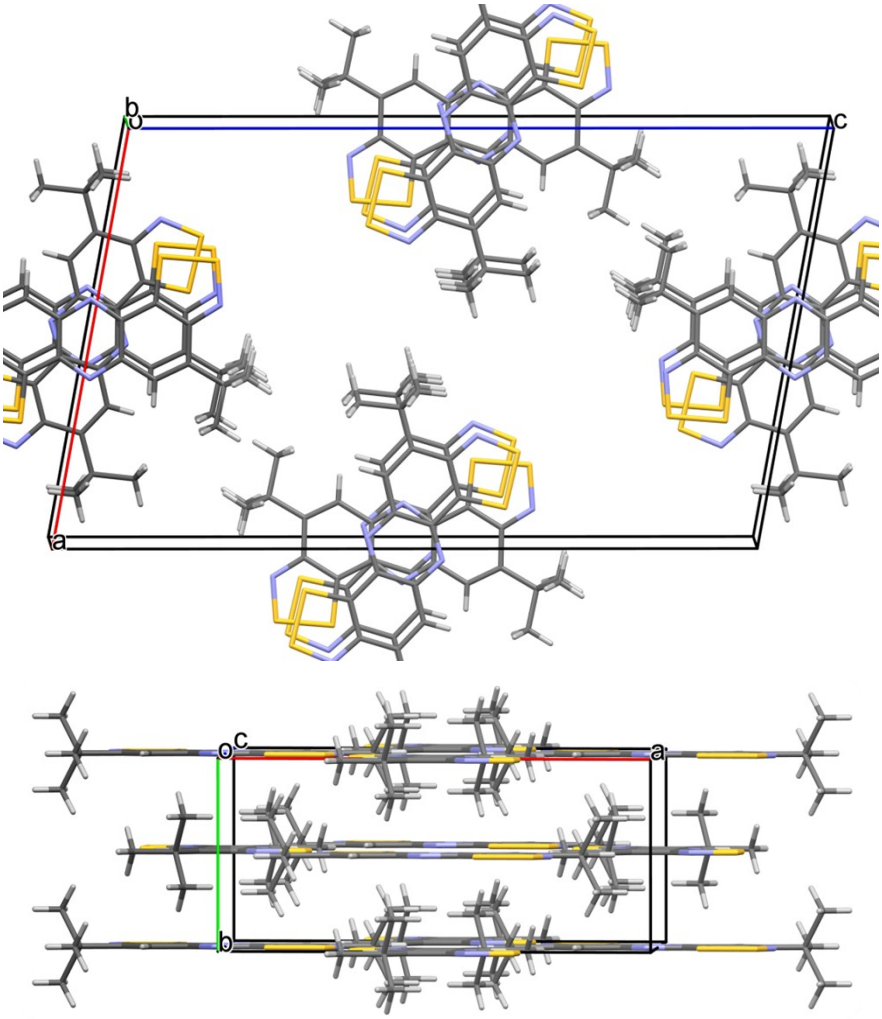

Figure S4. Packing of radical cations $[\mathbf{1}]^{\bullet+}$ in crystals of $[\mathbf{1}]^{\bullet+}[GaCl_4]^-$ (anions omitted).

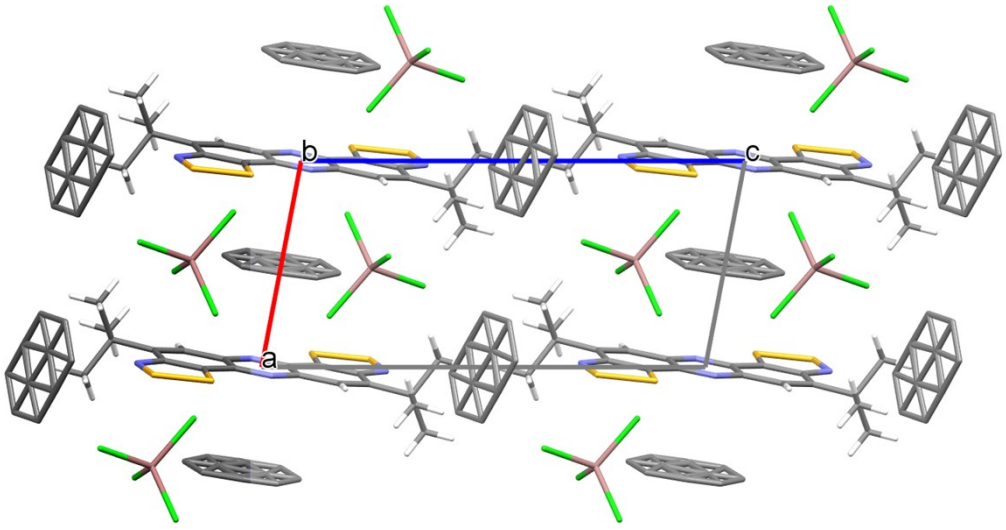

Figure S5. Packing of dications $[\mathbf{1}]^{2+}$ in crystals of $[\mathbf{1}]^{2+}[GaCl_4]^-_2 \cdot 2CH_3C_6H_5$ (disordered toluene molecules shown without H atoms and CH_3 groups).

In the crystals of $[\mathbf{3}]^{2+}[GaCl_4]^{-}_2$, the dications $[\mathbf{3}]^{2+}$ are perfectly planar except CH_3 groups. Geometries of its heterocycles are typical for Herz cations whose carbon-carbon bonds are alternated.[8] The presence of two 1,2,3-dithiazolium heterocycles in $[\mathbf{3}]^{2+}$ results in shortening of the bond C4–C5 to 1.359 and 1.375 Å in $[\mathbf{3}]^{2+}[GaCl_4]^{-}_2$ and $[\mathbf{3}]^{2+}[CF_3SO_3]^{-}_2$, respectively, in front of elongating of other carbon-carbon bonds to 1.417-1.461 Å.

4. Thermogravimetry and differential scanning calorimetry

The simultaneous thermogravimetry and differential scanning calorimetry (TG and DSC, respectively; Figures S6 and S7, Table S3) measurements were carried out with a Netzsch STA 409 instrument. Temperature and heat flow calibration was performed according to ISO 11357-1 standard by the temperatures and enthalpies of phase transitions of standard substances from the Netzsch calibration set (C_6H_5COOH (99.5%), $RbNO_3$ (99.99%), In (99.99%), Sn (99.99%), Bi (99.9995%) and Zn (99.999%). Samples of compounds (1 mg) were placed in aluminum crucibles (V = 25 µl, d = 6 mm) with pierced lid and heated at a heating rate of 10 or 50 $^{o}C\ min^{-1}$ in an inert (100% He) or oxidizing (20% O_2, 80% He) atmosphere. The obtained data were processed using *Netzsch Proteus Thermal Analysis* software. Temperature of maximal rate of decomposition (T_{max}) was determined from thermal analyses diagrams.

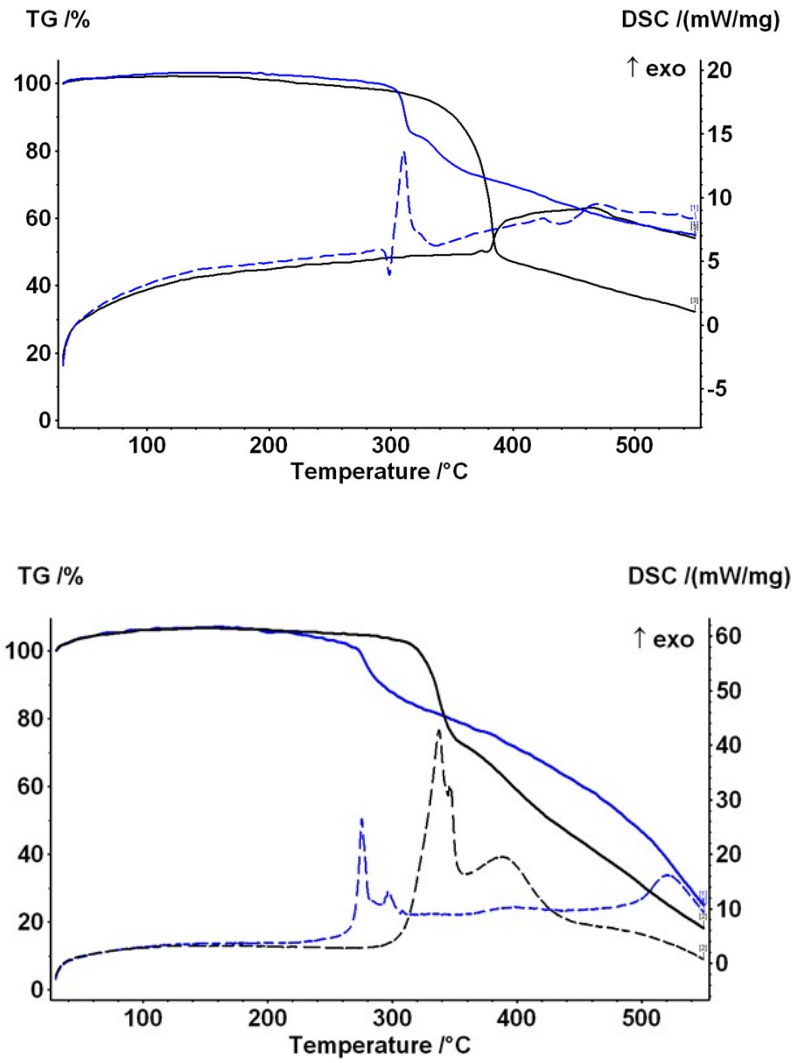

Figure S6. DSC (dotted) and TG (solid) curves of compounds **1** (black) and **2** (blue) at a heating rate 10 $^{o}C\ min^{-1}$ in inert (100% He; above) and oxidizing (20% O_2, 80% He; below) atmosphere.

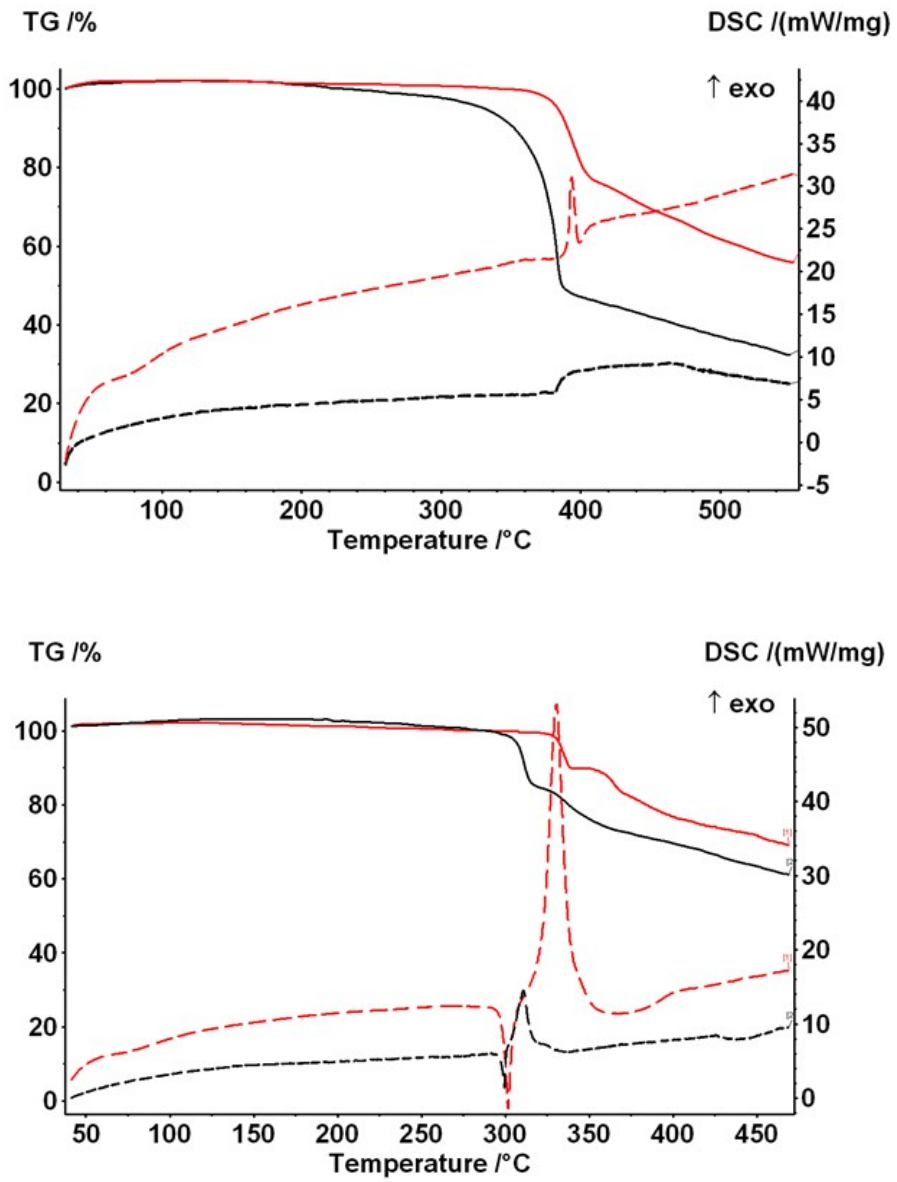

Figure S7. DSC (dotted) and TG (solid) curves of compounds **1** (above) and **2** (below) at a heating rate 10 (black) and 50 ^{o}C min^{-1} (red) in inert (100% He) atmosphere.

Table S3. The decomposition temperature T_d, the temperature of maximal rate of decomposition T_{max}, and the thermal effect of decomposition ΔH_d.

Compound	Atmosphere	T_d, °C	T_{max}, °C	ΔH_d	Number of decomposition steps
1	100% He	371	383	exo	2
	80% He, 20% O_2	325	337	exo	2
2	100% He	307	311	exo	3
	80% He, 20% O_2	271	277	exo	3

5. Quantum chemical calculations

Optimized geometries and hfc constants of radical ions of compounds **1** and **2** were calculated at the UB3LYP/6-31+G(d,p) level of theory[9] with the *GAMESS* program.[10]

Positions of the maxima and oscillator strengths in UV-Vis spectra of studied compounds were calculated with the *ORCA* 4.0.1 suit of programs[11] using TD-DFT[12] at the TD-B2PLYP/def2-tzpv level of theory[13] for the geometries optimized at the (U)PBE0/def2-tzpv level.[14,15] The solvents were taken into account using PCM model[16] with non-electrostatic terms of SMD model.[17]

Vibrational progression in the UV-Vis spectrum of compound **1** was calculated using the Frank-Condon and Heller approximations with the *orca asa* module[18] as implemented in the *ORCA* package.[11] In this approach, the energy of a vertical electron excitation E_0 is computed by TD-DFT[12], and the excited state energy gradient is estimated numerically with respect to each totally symmetric vibrational mode. The Huang-Rhys dimensionless parameter $S = \alpha(\Delta Q)^2/2$ (with ΔQ being dimensionless displacement of the excited state minimum along the normal mode, $\alpha = M\omega/\hbar$, and the reduced mass of the molecule M) was computed from the gradient under assumption that the excited state has the same hessian as the ground state. The Huang-Rhys parameter defines the relative intensities of the transitions in the progression at zero-temperature with corresponding Frank-Condon factors for a particular vibration

$$F_n^0 = \frac{e^{-S}S^n}{n!}$$

where n is the vibrational quantum number of the final state (n = 0, 1, 2, …).[19] The width of individual bands was chosen to be 500 cm^{-1}. The finite temperature and contributions from different vibrations onto the lines shape were taken into account by the independent mode displaced harmonic oscillator IMDHOT model.[20]

6. UV-Vis spectroscopy

UV-Vis spectra were collected with a Varian Cary 5000 spectrophotometer and calculated at the TD-B2PLYP/def2-tzvp and TD-BP86/def2-tzvp levels of theory (Figures S8-S15, Table S4).

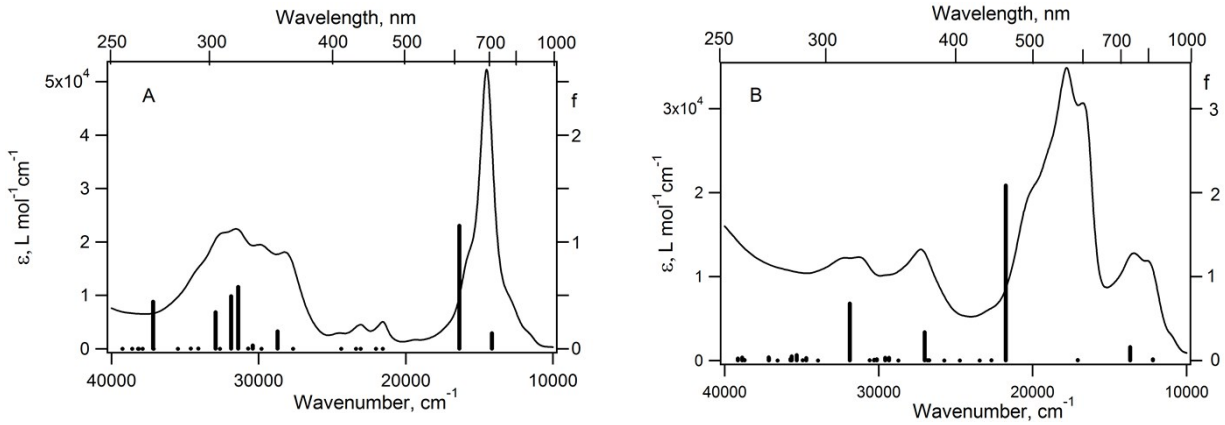

1 **2**

Figure S8. Experimental UV-Vis spectra of compounds **1** and **2** in $CHCl_3$ solutions (curves) and positions and oscillator strengths of the electronic transitions (vertical bars) calculated at the TD-DFT/B2PLYP/def2-tzvp level of theory for the PBE0/def2-tzvp optimized geometries. The solvent was accounted using PCM model with non-electrostatic terms of SMD model.

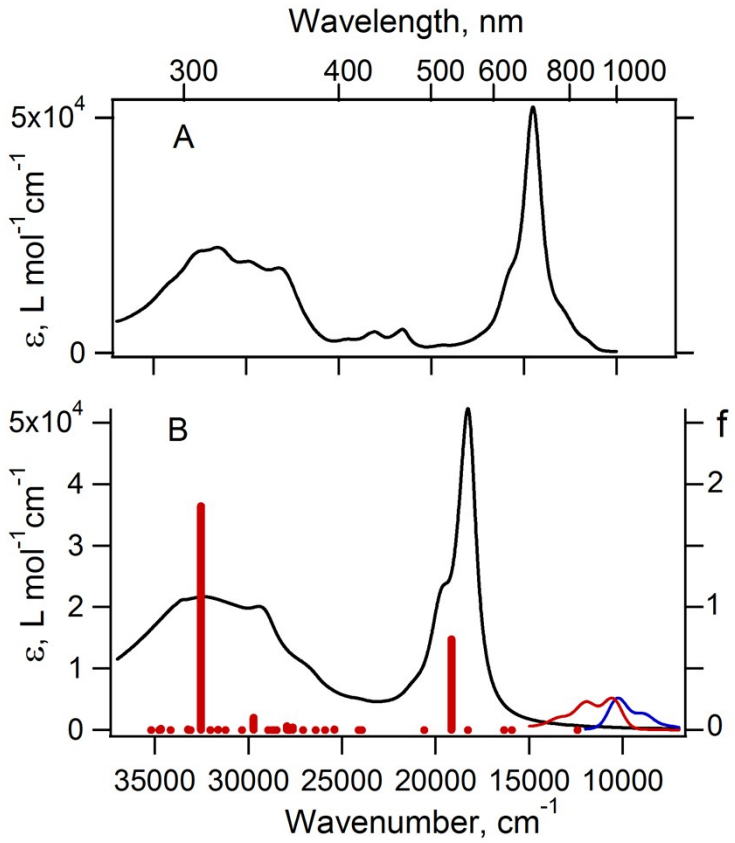

Figure S9. Experimental (A) and TD-BP86/def2-tzvp calculated (B) UV-Vis spectra of compound **1** in $CHCl_3$ solution. The red vertical bars indicate the calculated positions and oscillator strengths of the electronic transitions. Red curve corresponds to the long-wavelength band computed using the Frank-Condon and Heller approximations and multiplied by a factor of 10^6. Blue curve is a computed fluorescence spectrum of compound **1**. The geometry of compound **1** was optimized at the PBE0/def2-tzvp level of theory with accounting solvent via PCM model with non-electrostatic terms of SMD model.

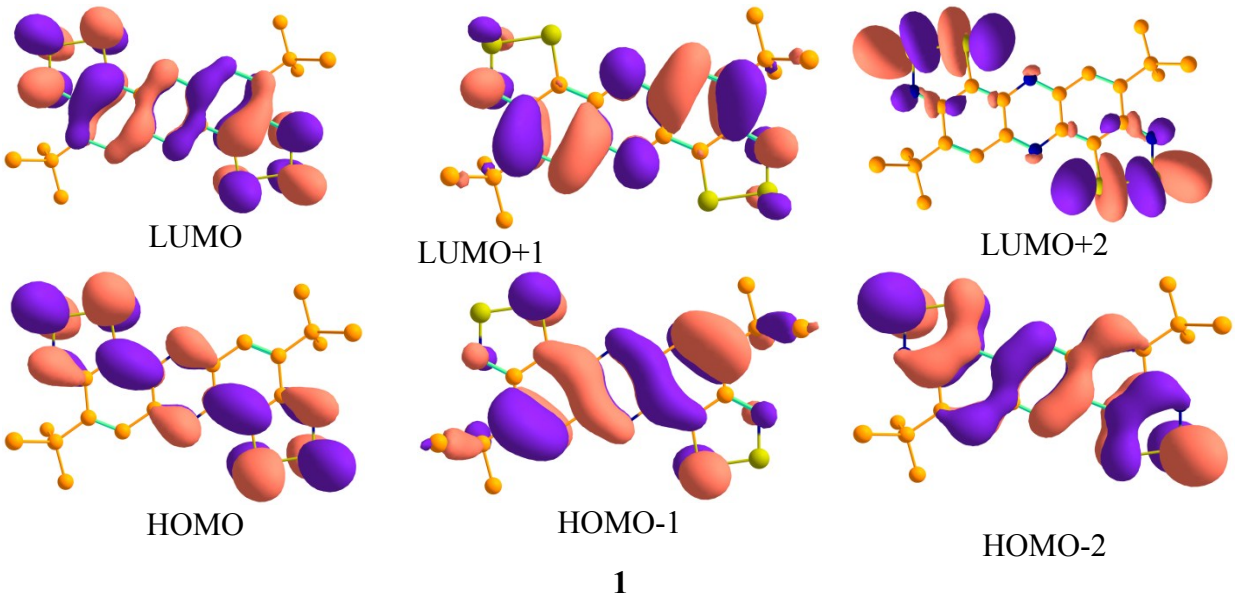

1

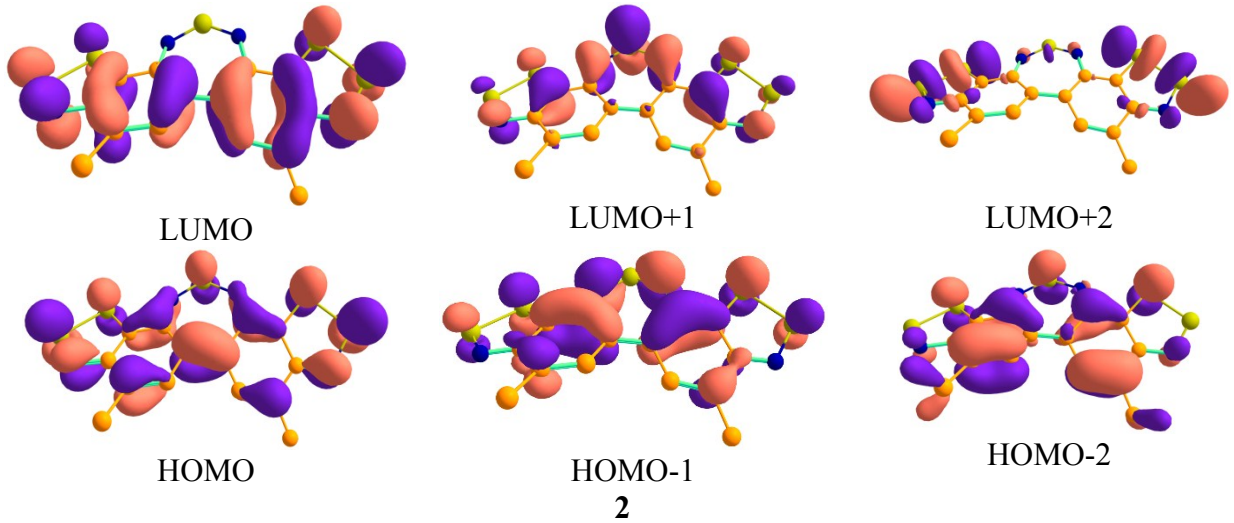

2

Figure S10. The frontier π-MOs of compounds **1** and **2** together with nearest occupied and virtual π-MOs calculated at the B2PLYP/def2-tzvp level of theory.

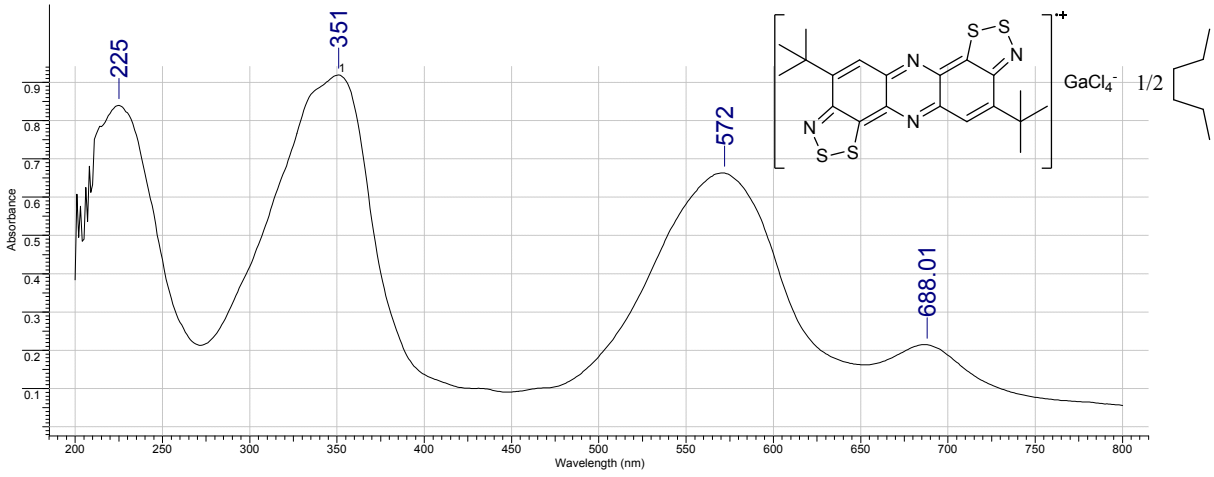

Figure S11. UV-Vis spectrum of $[\mathbf{1}]^{\bullet+}[GaCl_4]^-$ (solvate with hexane) in THF solution, absorption band at 688 nm belongs to minor admixture of compound **1**.

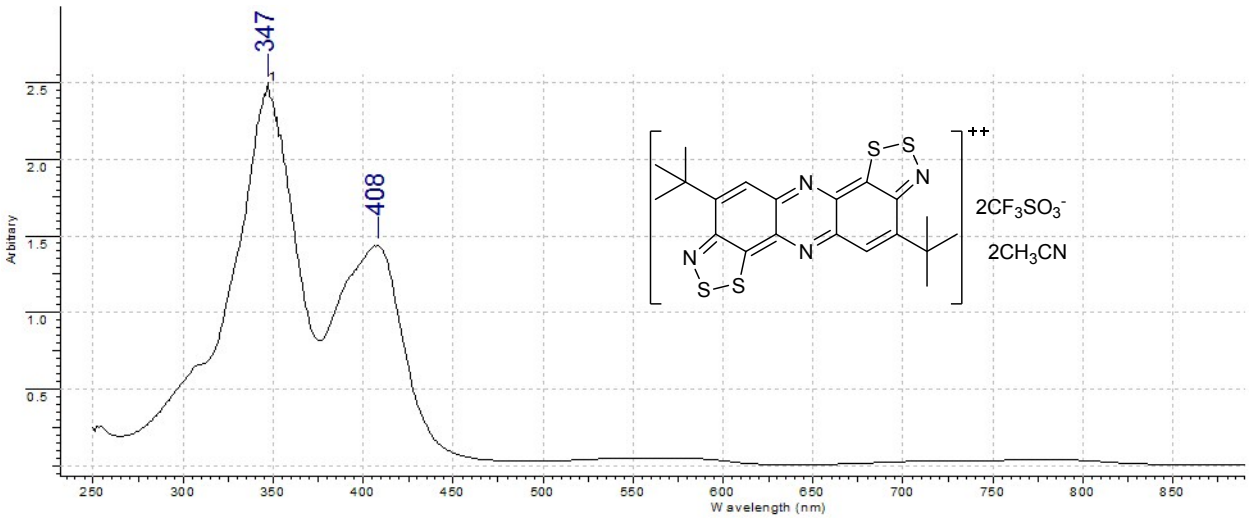

Figure S12. UV-Vis spectrum of salt $[\mathbf{1}]^{2+}[CF_3SO_3]^{-}_2$ (solvate with MeCN) in CF_3CO_2H.

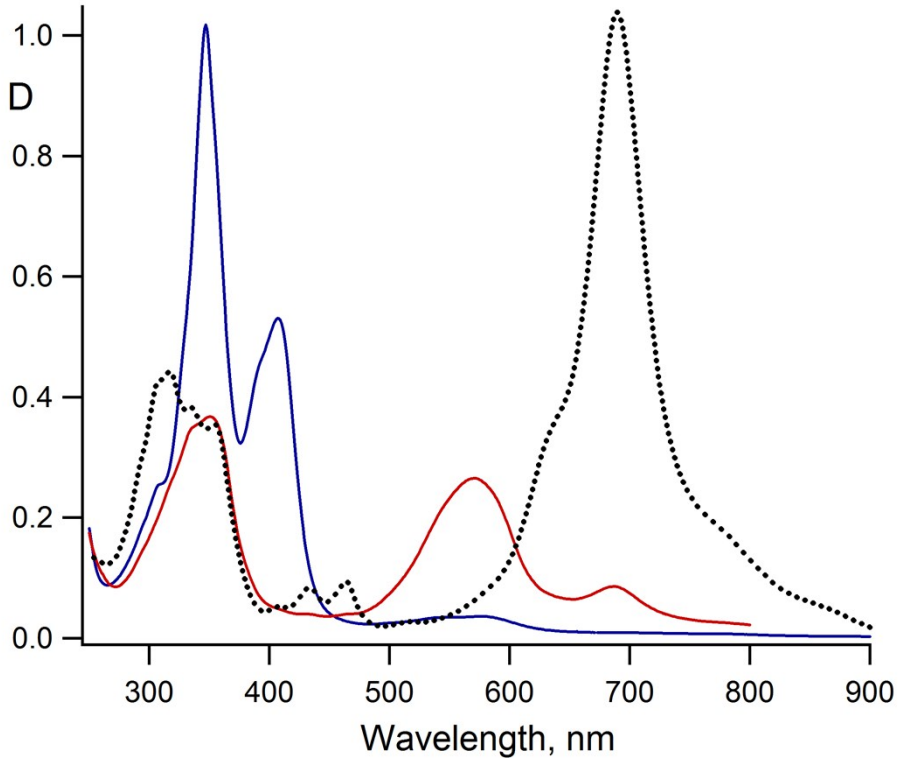

Figure S13. UV-Vis spectra of compound **1** (black dotted line) and salt $[\mathbf{1}]^{\bullet+}[GaCl_4]^{-}$ (red line) in THF solutions, and the spectrum of salt $[\mathbf{1}]^{2+}[Cl]^{-}_2$ (blue line) in CF_3CO_2H solution. All spectra were measured at C = 10^{-4} M with the 0.2 cm cell.

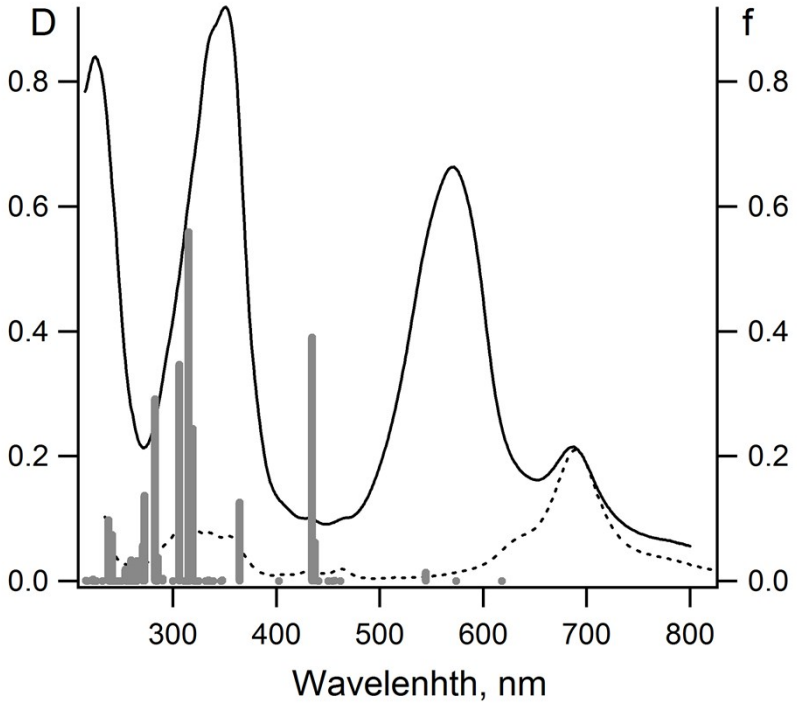

Figure S14. UV-Vis spectra of salt $[\mathbf{1}]^{\bullet+}[GaCl_4]^-$ (solid line) and compound **1** (dotted line) in THF solutions, and positions and oscillator strengths of electronic transitions of $[\mathbf{1}]^{\bullet+}$ calculated at the TD-B2PLYP/def2-tzvp level of theory (vertical bars).

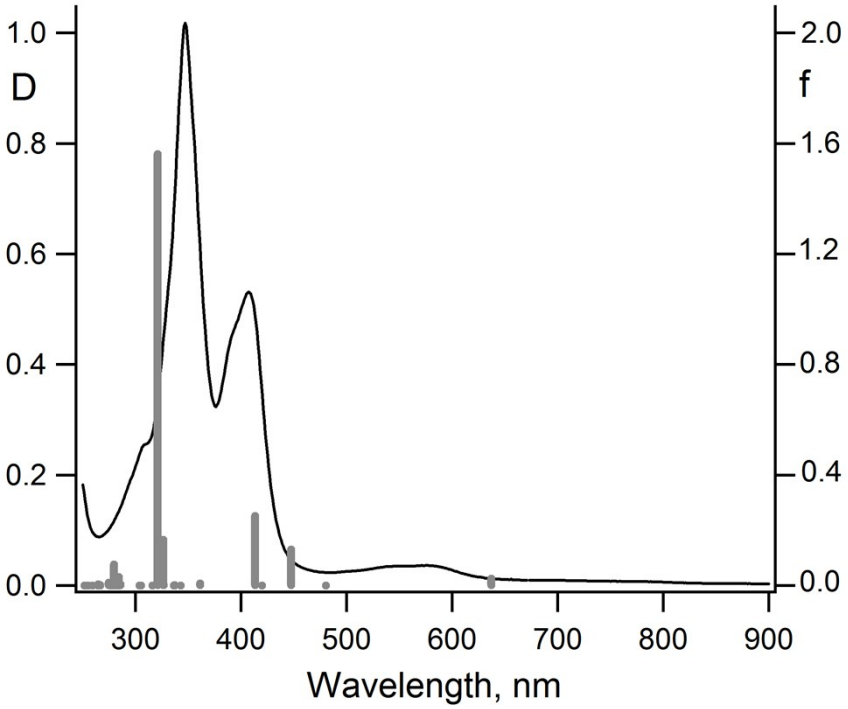

Figure S15. UV-Vis spectrum of $[\mathbf{1}]^{2+}[Cl]^-_2$ in CF_3CO_2H (solid line) and positions and oscillator strengths of electronic transitions calculated for dication of compound **1** at the TD-B2PLYP/def2-tzvp level of theory (vertical bars).

Table S4. Positions (λ_{max}, nm) and oscillator strengths (f) of electronic transitions for molecular ions of compound **1** calculated at the TD-B2PLYP/def2-tzvp level with account of THF solvent using PCM model with non-electrostatic terms of SMD model. Geometries of all species were optimized at the PBE0/def2-tzvp level of theory taking THF solvent into account. Only electronic transitions with $f \geq 0.01$ are presented.

Molecular ion							
$[\mathbf{1}]^{\bullet-}$		$[\mathbf{1}]^{\bullet+}$		$[\mathbf{1}]^{2-}$		$[\mathbf{1}]^{2+}$	
λ_{max}	f	λ_{max}	f	λ_{max}	f	λ_{max}	f
982.6	0.319	1136.9	0.295	2878.6	0.074	637	0.026
956.1	0.055	555.8	0.014	438.6	0.023	447.2	0.130
387.2	0.031	437.8	0.072	412.6	0.278	413.3	0.252
384.5	0.102	438.4	0.373	361.2	1.277	321	1.562
348.8	0.128	367.2	0.141	397.1	0.196	326.2	0.166
318.6	0.386	324.7	0.361	398.5	0.281	284	0.031
373.8	0.108	304.6	0.207	251.6	0.078	279.6	0.076
339.1	0.4398	314.5	0.617	247.6	0.010	274.5	0.010
315.8	0.188	316.8	0.015	249.5	0.087	244.6	0.148
329.2	0.010	286.8	0.232	231	0.370	239.1	0.048
294.4	0.061	272.5	0.105	224.2	0.016	243	0.122
280.3	0.099	289	0.040	240.5	0.354	231.8	0.024
246.4	0.088	277.1	0.075	217.3	0.208	231.6	0.112
284.2	0.190	263.1	0.025	213.3	0.040	222.2	0.199
256.8	0.025	265.1	0.032	209	0.018	216.3	0.240
237.8	0.013	244.5	0.087			229.2	0.016
258.3	0.049	240.4	0.029			215.7	0.063
243.5	0.044	249.7	0.031			222.4	0.084
235.8	0.055	239.5	0.069			208.3	0.016
234.8	0.058	229.5	0.451				
222.2	0.01697	222.7	0.01879				
223.8	0.03344						
217.3	0.36621						

7. Cyclic voltammetry

The CV measurements (Table S5, Figure S16) on compound **1** in THF (1 mM solution) were performed under nitrogen at 298 K with a PGSTAT 101 potentiostat (Metrohm Autolab). TSC 1600 closed electrochemical cell with solution volume of 1 mL connected to the potentiostat with a three-electrode scheme was employed. The cell was equipped with a stationary Pt mini-electrode (A = 4.9·10^{-4} cm^2). An Ag/AgCl pseudo-reference electrode was used as a reference. All manipulations with the cell were performed under nitrogen in a glovebox. The peak potentials obtained with the Ag/AgCl pseudo-reference electrode were recalculated versus a saturated calomel electrode (SCE). Potential difference for the reference electrodes was –0.231 V.

Also, CV measurements (Table S5, Figures S16 and S17) on compounds **1** and **2** in THF and DMF (1.5 mM solutions) were performed using a standard glass electrochemical cell with solution volume of 5 mL equipped with a stationary Pt disc electrode (A = 0.064 cm^2). Pt helix was used as an auxiliary electrode. A PG 310 USB potentiostat (HEKA Elektronik GmbH, Germany) was used for the measurements. The cell was connected to the potentiostat with a three-electrode scheme. Peak potentials were quoted with reference to a SCE. A bridge with 0.1 M of supporting electrolyte in THF or DMF was used to connect the cell and SCE. The supporting electrolytes were 0.1 M solutions of [n-Bu_4N][PF_6] and [Et_4N][ClO_4] for THF and DMF, respectively.

Digital simulations of CVs of compounds **1** and **2** in THF (Table S6) were carried out with the *Electrochemical Simulation Package* (ESP, v.2.4) designed by Carlo Nervi, Università di Torino, Italy. For multi-parametric optimizations, the *Simplex* algorithm was used as implemented in the package.

Pure resistances of the cell measured with INSTEK impedance meter were: 9340 Ω for the solution of supporting electrolyte in THF and 1050 Ω for the solution of supporting electrolyte in DMF at 298 K.

CV measurements on salt [**3**]$^{2+}$[CF_3SO_3]$^{-}_2$ (Figure S17) were performed by the same methods.

To avoid ambiguity in CV peak assignment, the *ijk* symbolism was used where i is a number of CV peak; j = A or C indicates anode or cathode branch of the CV curve, respectively; and k = (+) or (–) shows areas of positive or negative potentials, respectively. The designation of the corresponding peak potential is E_p^{ijk}.

7.1. Compounds 1 and 2

Table S5. Peak potentials of electrochemical reduction and oxidation of compounds **1** and **2**.[a,b]

Comp.	Solvent		Potential, V						
		i	Negative (–)				Positive (+)		
			1	2	3	4	1	2	3
1	THF	E_p^{iC}	–0.69	–1.29	–	–	0.64	0.75	–
		E_p^{iA}	–0.63	–1.18	–0.87	–0.24	0.71	0.81	–
	DMF	E_p^{iC}	–0.68	–1.27	–	–	0.43	0.59	–
		E_p^{iA}	–0.62	–1.17	–0.88	–0.29	0.49	0.65	–
2	THF	E_p^{iC}	–0.68	–1.25	–	–	0.69	0.50	0.36
		E_p^{iA}	–0.60	–1.09	–	–	0.76	–	–
	DMF	E_p^{iC}	–0.69	–1.25	–0.88	–1.50	0.34	0.51	0.17
		E_p^{iA}	–0.63	–1.17	–	0.16	0.55	0.59	–

[a] Potentials vs. SCE are measured at $\nu = 0.1$ V·s^{-1}; those in THF are *IR*-compensated; *i* is a number of peak in the corresponding CVs (Figures S16-S18), symbols A and C indicate anode or cathode branch of CV curve, respectively.

[b] Potentials of peaks 5C$^{(-)}$, 6C$^{(-)}$ and 5A$^{(-)}$ in the CV of **1** in THF (Figure S16*a*) are –1.95, –2.08 and –1.48 V, respectively, at $\nu = 0.1$ V·s^{-1}.

Table S6. Parameters of CV simulations of electrochemical reduction of compounds **1** and **2** in THF.[a]

C, mM		$D\times10^5$ cm^2·s^{-1}			S	$E^S_{1/2}$, V	k^S_e, cm·s^{-1}	k_f, s^{-1}
EE process for compound **1**								
1	**1**	[**1**]$^{\bullet-}$	[**1**]$^{2-}$	P[b]				
0.82	0.96	***1***	***1***	–	1	–0.655	0.0601	—
					2	–1.249	0.0225	
EC process for compound **2**								
2	**2**	[**2**]$^{\bullet-}$	–	P				
0.30	0.95	***1***	***1***	***1***	1	–0.646	0.0600	0.045
E process for compound **2**, model case								
2	**2**	[**2**]$^{\bullet-}$	–	P				
	0.95	***1***	***1***	***1***	1	–0.646	***0.0600***[c]	0

[a] Experimental and fixed values are given by bold italic, other values are optimised. S is a number of electrochemical (one-electron transfer) stage; $E^S_{1/2}$ are half-wave potentials for one-electron stage number S; k^S_e are heterogeneous electron-transfer constants for the stage S; k_f is rate constant of non-electrochemical irreversible reaction for EC process. Electron transfer coefficients (α) were assumed to be 0.5 for all electrochemical stages.

[b] P is the decay product of [2]$^{\bullet-}$.

[c] For the model case, k^S_e was fixed as for EC process.

Simulation of the CV curve for the EE-type reduction of compound **1** in THF (Figure S16b) showed that optimized k^1_e value relates to reversible electron transfer, whereas k^2_e value to quasi-reversible process in accordance with the proposed criterion ($0.03\nu^{1/2} \geq k_e \geq 0.000025\nu^{1/2}$).[21] From kinetic point of view, therefore, the first step of electrochemical reduction of compound **1** is reversible one-electron transfer, whereas the addition of electron to [**1**]$^{\bullet-}$ with the formation of [**1**]$^{2-}$ is quasi-reversible process.

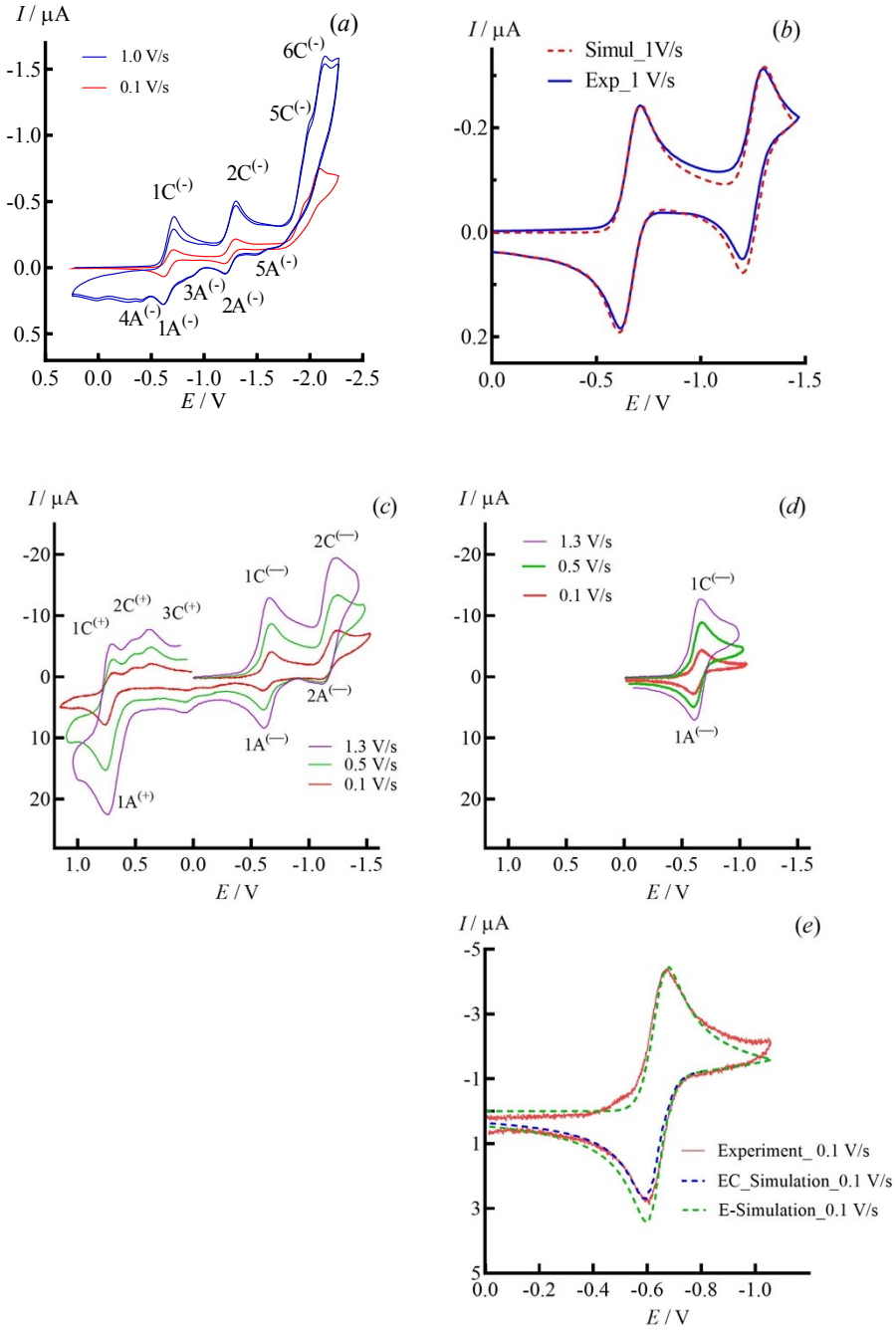

Figure S16. CVs of compounds **1** and **2** in THF referred to SCE. Compound **1**, Pt working electrode (A = 4.9·10^{-4} cm^2): (*a*) potential sweep range 0.25 > E > –2.3 V, potential sweep rate ν = 0.1 V s^{-1} (red line) and 1.0 V s^{-1} (blue line); (*b*) potential sweep range 0.0 > E > –1.5 V at ν = 1.0 V s^{-1} (solid blue line – experiment, dotted red line – simulation). Compound **2**, Pt working electrode (A = 0.069 cm^2): (*c*) potential range 1.25 > E > –1.60 V at various ν indicated by colour; (*d*) potential range 0.0 > E > –1.60 V at various ν indicated by colour; (e) potential range 0.0 > E > –1.60 V (solid red line – experiment, dotted blue line – simulation in accordance with EC process, dotted green line – simulation in accordance with reversible E process; E – one-

electron transfer process, EC – one-electron transfer process accompanied by non-electrochemical irreversible transformation of formed species.

Comparative simulations of the first stage of electrochemical reduction compound **2** in THF according to the EC and E mechanisms demonstrated a better agreement of the EC-fitting to the experimental CV curve. The corresponding first-order rate constant of an irreversible non-electrochemical reaction following after the electron transfer is small, and the half-life time of $[\mathbf{2}]^{\bullet-}$ was found to be 15 s. This time is too short to observe $[\mathbf{2}]^{\bullet-}$ by EPR under the CV conditions especially in front of higher stability of paramagnetic product of its decay (see Section 8 below).

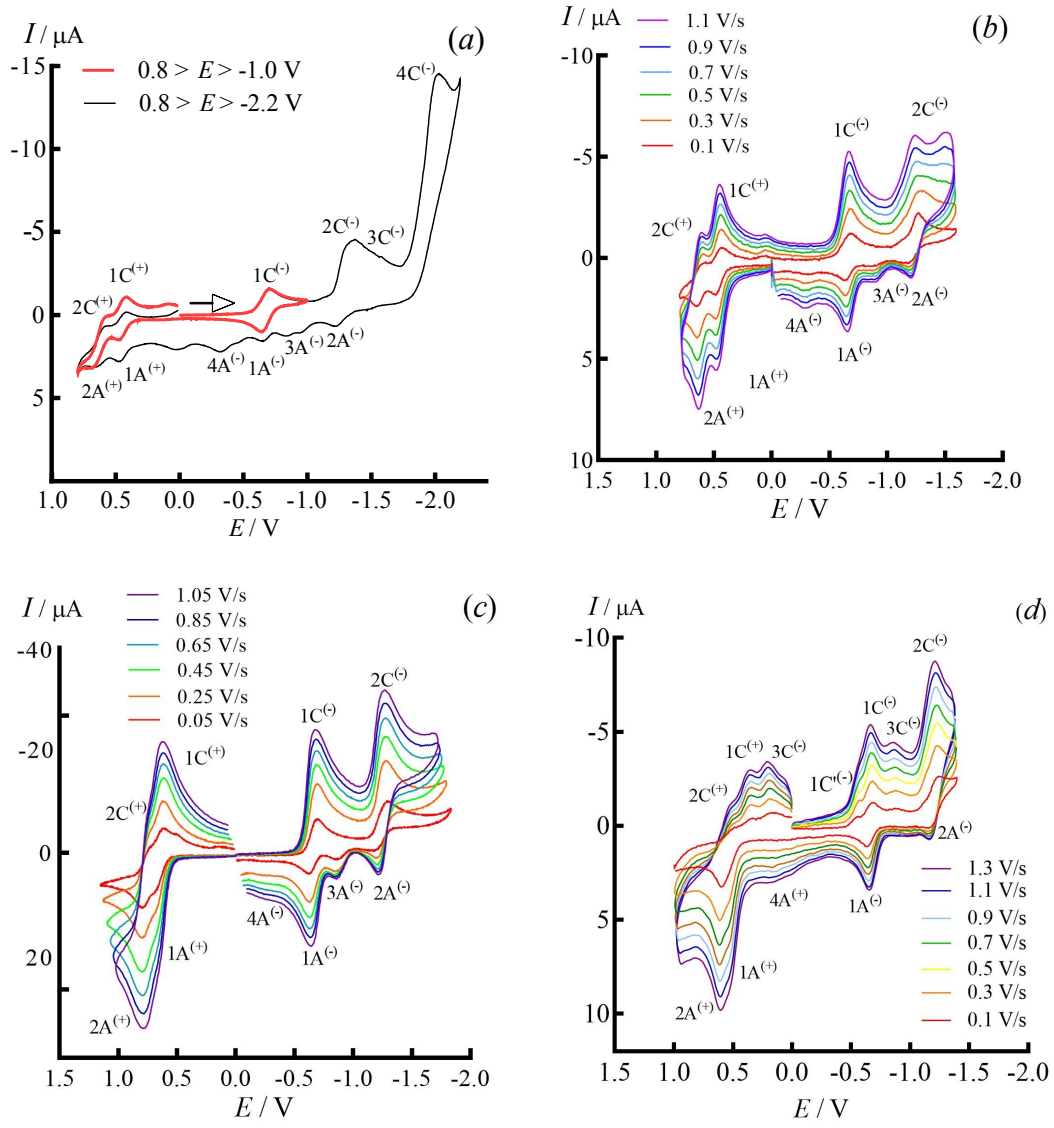

Figure S17. CVs of compounds **1** and **2** with Pt working electrode (A = 0.069 cm^2) vs. SCE. Compound **1**: (*a*) DMF solution, potential sweep ranges 0.7 > E > –2.3 V (black line) and 0.7 > E > –1.0 V (red line), potential sweep rate 0.1 V·s^{-1}; (*b*) DMF solution, potential sweep range 0.7

> E > –1.7 V at various potential sweep rates indicated by colors; (*c*) THF solution, potential sweep ranges 0.0 > E > –2.0 V and 1.2 > E > 0.0 V at various potential sweep rates indicated by colours. Compound **2**: (*d*) DMF solution, potential sweep range 1.0 > E > –2.0 V at various potential sweep rates indicated by colors. All shown CV curves are *IR*-compensated with pure resistance of the cell 1050 Ω for DMF and 9340 Ω for THF at 298 K, concentration of supporting electrolyte [n-Bu_4N][PF_6] 0.1 M for both solvents.

The first stage of the electrochemical reduction of compound **2** displayed an additional pre-peak 1C'$^{(-)}$ which disappeared under increased potential sweep rates, whereas peak 3C$^{(-)}$ was visible at all rates used. The adsorption nature can be assigned to the pre-peak 1C'$^{(-)}$, whilst the peak 3C$^{(-)}$ can be associated with electrochemical reduction of decomposition product of [**2**]$^{\bullet-}$. This explains why [**2**]$^{\bullet-}$ was not observed by EPR in DMF.

7.2. Salt $[3]^{2+}[CF_3SO_3]^{-}_2$

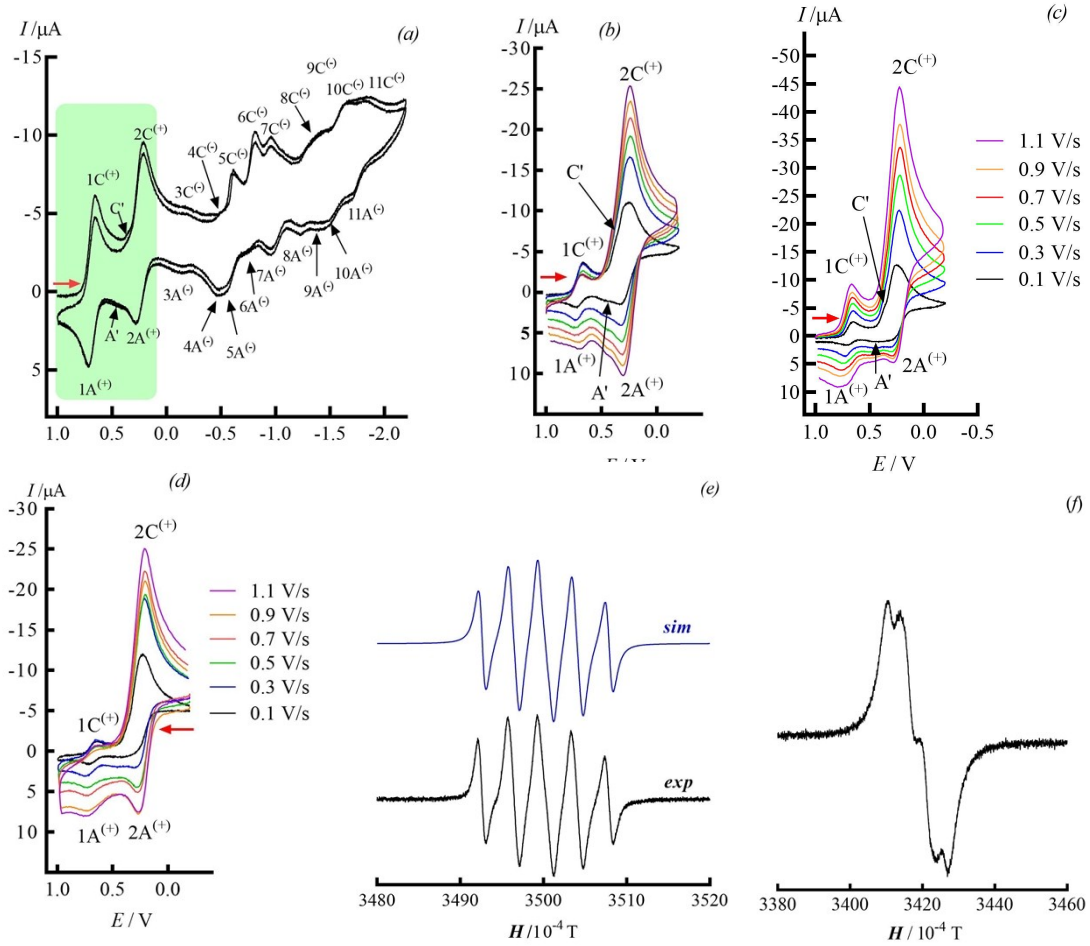

Figure S18. CV of $[\mathbf{3}]^{2+}[CF_3SO_3]^{-}_2$ in MeCN solution (0.1 M Et_4NClO_4; Pt working electrode, A = 0.069 cm^2; *vs* SCE) and EPR spectrum of $[\mathbf{3}]^{\bullet+}$.

Electrochemical reduction: (*a*) beginning of the experiment, 2 cycles, initial potential of 1.0 V, potential sweep range 1.0 > E > –2.2 V, v = 0.1 V s^{-1}; (*b*) 5 min after beginning of the experiment, 6 cycles, initial potential of 1.0 V, potential sweep range 1.0 > E > –0.2 V, 0.1 < v < 1.1 V s^{-1}; (*c*) 10 min after beginning of the experiment, 6 cycles, potential sweep range 1.0 > E > –0.2 V, 0.1 < v < 1.1 V s^{-1}; the solvent was bubbled with argon before each CV cycle.

Electrochemical oxidation: (*d*) 15 min after beginning of the experiment, initial potential of –0.2 V, 6 cycles, potential sweep range –0.2 < E < 1.0 V, 0.1 < v < 1.1 V s^{-1}; red arrows indicate the direction of potential sweep.

EPR spectrum of $[\mathbf{3}]^{\bullet+}$: (*e*) obtained with electrochemical reduction of $[\mathbf{3}]^{2+}[CF_3SO_3]^{-}_2$ at the potential of peak 1C$^{(+)}$; (*f*) detected as paramagnetic admixture to $[\mathbf{3}]^{2+}[Cl]^{-}_2$ (solution in CF_3CO_2H; the spectrum is broadened due to exchange between radical cation $[\mathbf{3}]^{\bullet+}$ and dication $[\mathbf{3}]^{2+}$ and unchanged on dilution; large excess of $[\mathbf{3}]^{2+}$ suppresses disproportionation of $[\mathbf{3}]^{\bullet+}$.

Electrochemical reduction of $[\mathbf{3}]^{2+}[CF_3SO_3]^-_2$ in MeCN reveals two one-electron reversible peaks $1C^{(+)}$ (0.65 V) and $2C^{(+)}$ (0.21 V) in positive range of potentials corresponding to the formation of radical cation $[\mathbf{3}]^{\bullet+}$ and diradical **3**, respectively (Figure S18*a*). Dimerization of the diradical **3** with the formation of compounds **1** and **2** leads to appearance of a number of overlapping CV waves (peaks $3C^{(-)}$-$11C^{(-)}$ and $3A^{(-)}$-$11A^{(-)}$) in the negative range of potentials. Due to different solvents used for CV of $[\mathbf{3}]^{2+}[CF_3SO_3]^-_2$ (MeCN) and **1** and **2** (THF and DMF; the main text), it is impossible to assign certain peaks to reductive processes with **1** or **2**. The current of peak $1C^{(+)}$ decreases with each series of CV cycles due to subsequent chemical transformations of $[\mathbf{3}]^{\bullet+}$. The current of peak $2C^{(+)}$ is presumably controlled by both diffusion and adsorption as revealed by superposition with adsorptive CV wave (peaks C'-A', Figure S18*b,c*). No adsorption peaks were observed on oxidative CVs of $[\mathbf{3}]^{2+}[CF_3SO_3]^-_2$ in the potential sweep range $-0.2 < E < 1.0$ V with the initial potential of –0.2 V (Figure S18*d*).

EPR spectrum of $[\mathbf{3}]^{\bullet+}$ generated by electrochemical reduction of $[\mathbf{3}]^{2+}[CF_3SO_3]^-_2$ in MeCN at the potential of peak $1C^{(+)}$ reveals two hfc with ^{14}N (4.13 and 3.50 G) and a hfc with ^{1}H (0.23 G) nuclei obtained by simulation of the spectrum with the *Winsim 2002* program. Fast irreversible dimerization of diradical **3** hampers its EPR detection.

8. Electron paramagnetic resonance spectroscopy

EPR spectra of radical ions of compounds **1** and **2** (Figures 2 and 4 of the main text; Figure S19, Table S7) were measured with an ELEXSYS E-540 spectrometer (X-band, MW frequency ~9.87 GHz, MW power 1 mW, modulation frequency 100 kHz, and modulation amplitude 0.006 mT) equipped with a high-Q cylindrical resonator ER4119HS. Measurements of g-factors of the radical ions were performed with a rectangle double X-band resonator ER4105DR with 2,2-diphenyl-1-picrylhydrazyl (g = 2.0036) as a reference. For the EPR measurements on the radical ions, stationary electrochemical reduction/oxidation of compounds **1** and **2** at corresponding peak potentials was carried out at 295 K under anaerobic conditions. Electrochemical cell for EPR measurements equipped with Pt working electrode was placed into the EPR cavity. Electrolysis was performed in dry THF and DMF with 0.1 M [n-Bu_4N][PF_6] (THF) and [Et_4N][ClO_4] (DMF) as supporting electrolytes. Simulations of the experimental EPR spectra were accomplished with the *Winsim 2002* program.[22] The *Simplex* algorithm was used for optimization of hfc constants and line widths. The accuracy in calculations of hfc constants and line widths was 0.001 G.

Table S7. Experimental and DFT-calculated isotropic hfc constants (G) of radical ions of compounds **1** and **2**.[a-c]

Radical ion	Solvent	Experiment	UB3LYP/6-31+G(d)
[**1**]$^{\bullet-}$	DMF	4.67 ($N^{3,9}$)	5.73 ($N^{3,9}$); –0.86 ($N^{6,12}$); 0.54 ($H^{5,11}$)
	THF	4.78 ($N^{3,9}$)	5.64 ($N^{3,9}$); –0.75 ($N^{6,12}$); 0.40 ($H^{5,11}$)
[**1**]$^{\bullet+}$	DMF	1.55 ($N^{3,9}$); 0.81 ($N^{6,12}$); 0.13 ($H^{5,11}$)	1.94 ($N^{3,9}$); 1.02 ($N^{6,12}$); 0.33 ($H^{5,11}$)
	THF	1.64 ($N^{3,9}$); 0.84 ($N^{6,12}$); ~0.07 ($H^{5,11}$)	1.94 ($N^{3,9}$); 1.03 ($N^{6,12}$); 0.32 ($H^{5,11}$)
[**2**]$^{\bullet+}$	THF	2.01 ($N^{3,8}$); 0.78 ($H^{5,6}$)	2.61 ($N^{3,8}$); 0.18 ($N^{11,13}$); 1.49 ($H^{5,6}$)

[a] Numbers of H atoms are the same as for C atoms they are bound with.

[b] PCM (SMD) model was used to describe the solvents. For radical ions of **1**, hfc constants with ^{14}N and ^{1}H nuclei are averaged according to their symmetry.

[c] For radical ions of **1**, g factors are 2.0073 and 2.0098 for the anion and cation respectively.

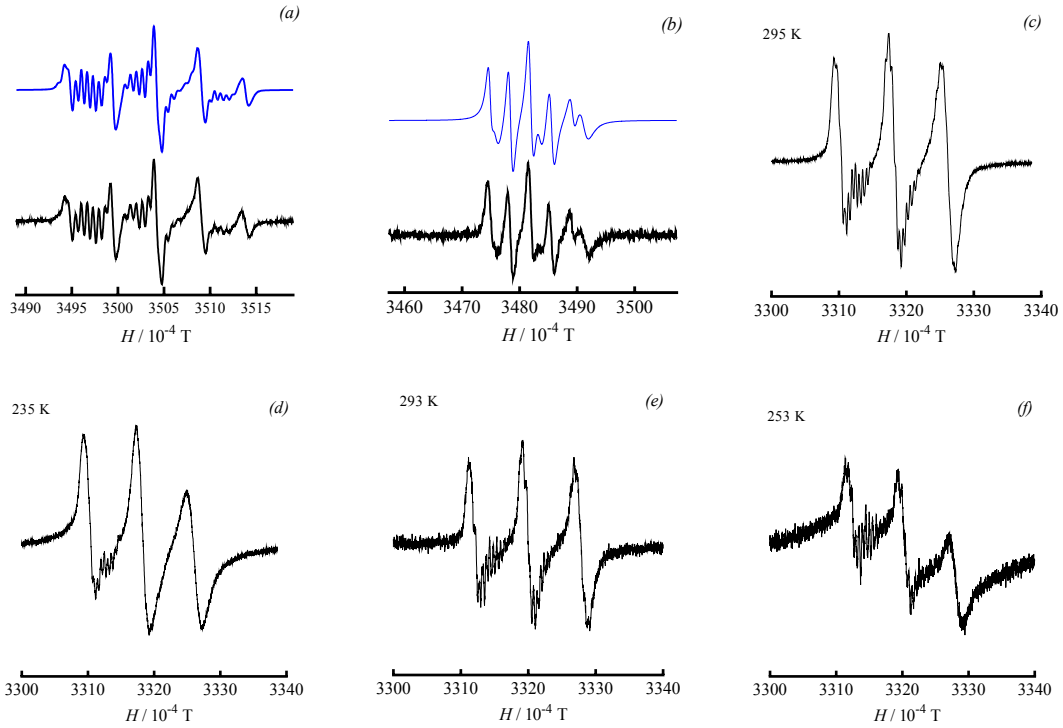

Figure S19. Superimposed EPR spectra in THF: (*a*) radical anion of compound **1** and another paramagnetic specie **R1** observed under conditions of electrochemical reduction of **1** at electrolysis potentials $E > E_p^{2C(-)}$ (black curve – experiment, blue curve – simulation); (*b*) radical cation $[\mathbf{2}]^{\bullet+}$ and another paramagnetic specie **R2** observed under conditions of electrochemical oxidation of **2** at $E = E_p^{2A(+)}$ (black curve – experiment, blue curve – simulation). EPR spectra observed under conditions of electrochemical reduction of compound **2** at various temperatures in THF and DMF solutions: (*c*) THF, 295 K; (*d*) THF, 235 K; (*e*) DMF, 293 K; (*f*) DMF, 253 K.

Table S8. Hfc constants (G) of paramagnetic species **R1** and **R2** observed under conditions of electrochemical reduction of compound **1** in the range of electrolysis potentials $E > E_p^{2C(-)}$, and electrochemical oxidation of compound **2** at $E = E_p^{2A(+)}$, respectively.

Specie	Solvent	Hfc constants
R1	THF	6.59 (N_1), 1.26 (N_2), 0.66 (N_3), 0.12 (N_4), 1.18 (H_1), 0.69 (H_2), 0.49 (H_3)
	DMF	6.28 (N_1), 1.34 (N_2), 0.60 (N_3), 0.13 (N_4), 1.21 (H_1), 0.70 (H_2), 0.55 (H_3)
$[\mathbf{2}]^{\bullet+}$ [a]	DMF	3.48 ($N^{3,9}$), 0.35 ($H^{5,11}$)
R2[a]		7.65 (N_1)

[a] EPR spectrum of **R2** was optimized with line widths of triplet resulting from hfc with ^{14}N nucleus. For the lines of quantum numbers M_N = (1, 0, –1) the corresponding widths are equal to 1.36, 1.28 and 1.60 G, respectively. EPR spectrum of $[\mathbf{2}]^{\bullet+}$ was optimized with line widths of 0.58 ± 0.13 G for quintet resulting from hfc with two ^{14}N nuclei.

9. Spectroelectrochemistry

Spectroelectrochemical measurements (Figures S20-S24) on compound **1** (0.16 mM solution in THF) were performed at 298 K. TSC spectroelectrochemical cell with solution volume of 0.5 mL and optical pathway of 2 mm was used. Pt mesh electrode was employed as a working electrode and an Ag/AgCl pseudo-reference electrode was used as a reference. n-Bu_4NPF_6 (0.1 M solution in THF) was used as a supporting electrolyte. All manipulations with the cell were performed under nitrogen in a glovebox. The cell was connected to a PGSTAT 101 potentiostat (Metrohm Autolab) via three-electrode scheme and simultaneously to an UV-Vis NIR spectrophotometer (Avantes) via a fiber optic line. Optical spectra were recorded in two modes: differential UV-Vis spectra [$(D - D_{blank})(\lambda)$, where D is absorption density and λ wavelength] were obtained when the solution of compound **1** in THF was taken as a blank; and normal UV-Vis spectra ($D(\lambda)$) were collected when the solution of supporting electrolyte in THF was taken as a blank. The potentiostat was synchronized with the spectrophotometer using the *Nova 2.1.2* software synchronized with the *AvaSoft 8.7* software. Both the softwares were used for simultaneous acquisition of optical and electrochemical data in a mode of staircase cyclic potential sweep. The final data analysis was carried out with the *Igor PRO 8.0* software.

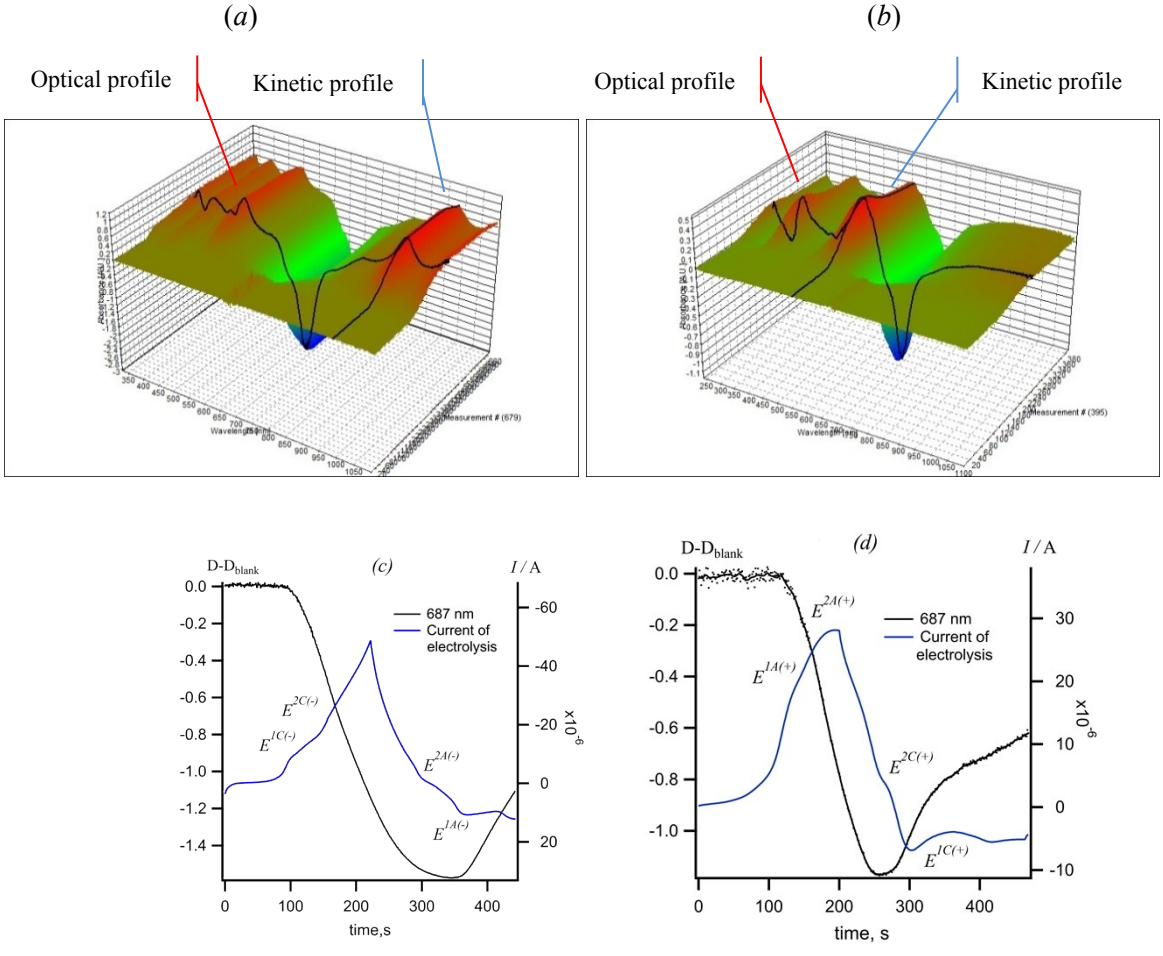

Figure S20. Differential spectroelectrochemical surfaces of compound **1** in THF for electrochemical reduction (*a*) and oxidation (*b*) and kinetics of characteristic absorption band of **1** at 688 nm (left axis). Corresponding electrolysis current time dependences for electrochemical reduction (*c*) and oxidation (*d*) of **1** (right axis).

Figure S21 displays: *(a)* Dependences $[(D - D_{blank})(t, \lambda)]$ registered at selected potential upon reduction of compound **1** using a negative potential sweep $E(t)$: $0.2 \rightarrow -2.0 \rightarrow -0.71$ V with $0 < t < 345$ s; transient differential UV-Vis spectra obtained are characterized by two negative absorption bands associated with decay of the neutral form of **1** and a series of the positive absorption bands associated with the formation of the negatively charged molecular ions of **1**.

(b) Kinetics of the absorption decay of the neutral form **1** (band at 687 nm) and the absorption growth associated with molecular ions; the former kinetics has a minimum at t = 345 s corresponding to the potential $E = -0.71$ V at the reverse branch of potential sweep. Delay in the absorption kinetics relative to the currents of cyclic macro-electrolysis is caused by the limitation of mass transport from the surface of the mesh working electrode into the solution volume.

(c) Assumption that electrolysis within time range $0 < t < 345$ s leads to complete decomposition of compound **1**, together with results of additional electrochemical reduction experiments, makes it possible to obtain UV-Vis spectra of the reduction products. The equilibrium constant of the disproportionation reaction $[\mathbf{1}]^{\bullet-} + [\mathbf{1}]^{\bullet-} \leftrightarrow \mathbf{1} + [\mathbf{1}]^{2-}$ can be estimated from the difference in the corresponding half-wave potentials ($E_{½}^{2C(-)} - E_{½}^{1C(-)}$) as 1.88×10^{-10} in THF. Thus, the equilibrium is significantly shifted towards the formation of $[\mathbf{1}]^{\bullet-}$ and the UV-Vis spectrum presented in Figure S21*c* (red line, normal $D(\nu)$ mode where ν is wavenumber) can be assign mainly to this radical anion. Indeed, the spectrum agrees reasonably well with the electronic transitions calculated for $[\mathbf{1}]^{\bullet-}$ at the TD-B2PLYP level of theory. Particularly, the structured band in the near-IR region agrees well with calculated intense absorption at 983 nm. The broad absorption with maximum at 340 nm and shoulders at 285 and 385 nm is also in agreement with a series of calculated transitions.

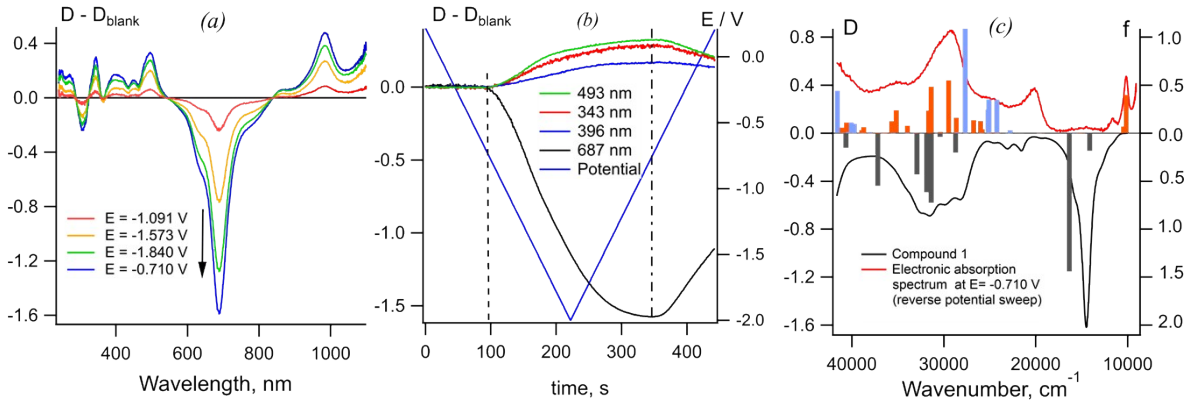

Figure S21. (*a*) Transformations of the differential UV-Vis spectrum of compound **1** during its electrochemical reduction in THF solution at 298 K. (*b*) Kinetics of the transient absorption at selected wavelengths (left axis) and time dependence of the potential sweep (right axis). (*c*) The UV-Vis spectra of the reduction products in THF registered at E = –0.71 V (red curve) and UV-Vis spectrum of **1** in THF at the beginning of electrochemical reduction (black curve, multiplied by –1). The vertical bars indicate the positions and oscillator strengths (right axis) of the electronic transitions calculated at the TD-BP86/def2-tzvp level of theory for **1** (black bars, multiplied by –1) and its radical anion (red bars) and dianion (blue bars).

Figure S22 displays: (*a*) Transient differential UV-Vis spectra registered at the selected potentials upon electrochemical oxidation of compound **1** with a positive potential sweep *E*(t): 0 → 1.0 → –0.3 V with 0 < t < 257 s. The spectra demonstrate three negative absorption bands associated with decay of **1** and three positive absorption bands associated with the formation of positively charged molecular ions of **1**.

(*b*) Kinetic curves of absorption decay and growth along with time profile of the potential. Similar to the electrochemical reduction, there is a delay of the absorption kinetics relative to the current of cyclic macro-electrolysis caused by the limitation of mass transport.

(*c*) Transient UV-Vis spectra represented in the D(ν) mode and corresponding to the maximal oxidation of compound **1** (red line) along with spectrum of **1** multiplied by –1 (black line). To facilitate the assignment of the transient spectra, UV-Vis spectra of authentic salts of $[\mathbf{1}]^{\bullet+}$ and $[\mathbf{1}]^{2+}$ were collected.

Comparison confirms that positive absorption bands in the transient UV-Vis spectra belong to $[\mathbf{1}]^{\bullet+}$. Moreover, comparison of the transient spectrum with UV-Vis spectrum of salt $[\mathbf{1}]^{2+}[CF_3SO_3]^{-}_2$ indicates a lack of noticeable contribution from $[\mathbf{1}]^{2+}$. This is in agreement with the low equilibrium constant of 0.017 (THF) calculated with electrochemical data for the disproportionation reaction $[\mathbf{1}]^{\bullet+} + [\mathbf{1}]^{\bullet+} \leftrightarrow \mathbf{1} + [\mathbf{1}]^{2+}$. Positions and oscillator strengths calculated for $[\mathbf{1}]^{\bullet+}$ and $[\mathbf{1}]^{2+}$ at the TD-B2PLYP level of theory are in reasonable agreement with the

experimental spectra of these species. Notably, in the spectrum of $[\mathbf{1}]^{\bullet+}$ there is a broad absorption band in the near-IR area which is in a good agreement with the TD-DFT calculations.

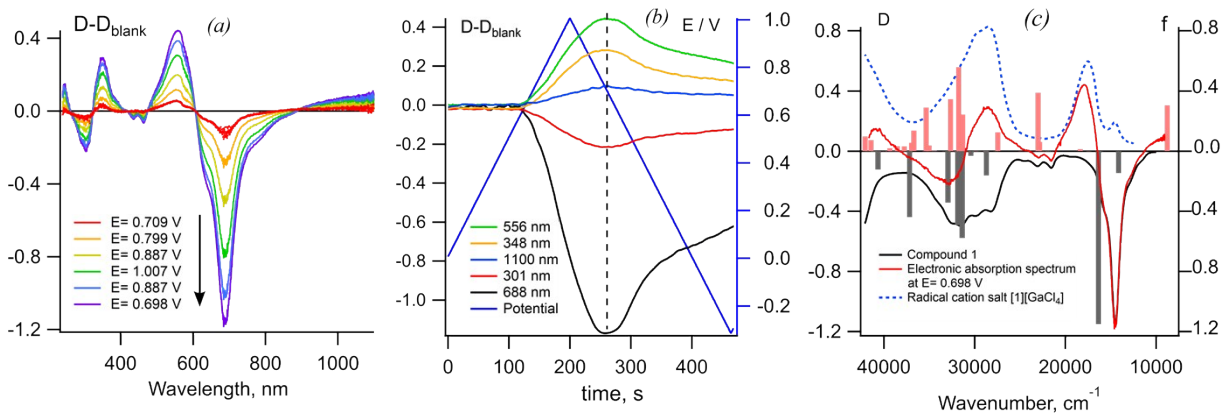

Figure S22. (*a*) Transformations of the differential UV-Vis spectrum of a solution of compound **1** in THF during its electrochemical oxidation at 298 K (the corresponding potentials are indicated by colors); (*b*) kinetics of various absorption bands (indicated by colors, left axis) and the corresponding potential sweep (right axis); (*c*) differential UV-Vis spectra at E = 0.698 V in THF (red curve), UV-Vis spectra of **1** (shown with negative absorption density) and its radical cation salt $[\mathbf{1}]^{\bullet+}[GaCl_4]^-$ in THF (blue dotted curve) together with positions and oscillator strengths (right axis) of electronic transitions of **1** (black bars) and $[\mathbf{1}]^{\bullet+}$ (red bars) calculated at the TD-B2PLYP/def2-tzvp level of theory.

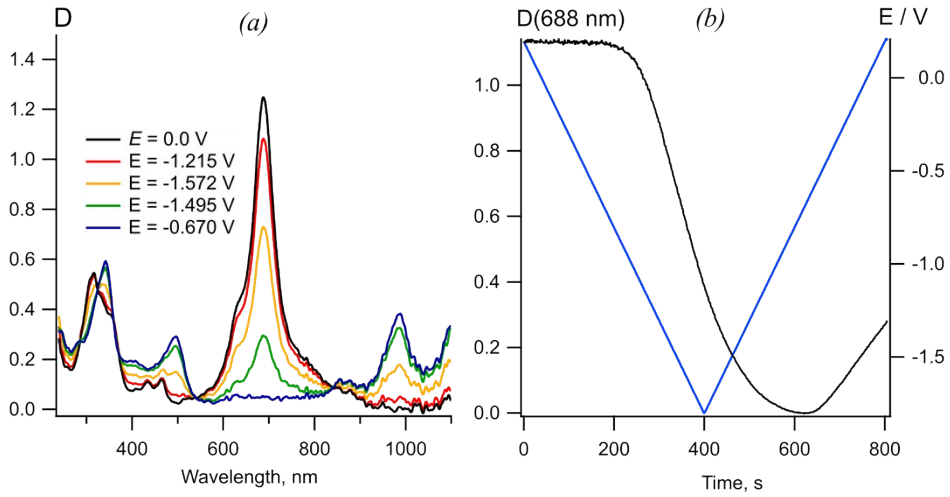

Figure S23. (*a*) Transformations of the UV-Vis spectra of compound **1** in THF solution upon its electrochemical reduction with potential sweep rate 5 mV·s^{-1}; (*b*) the corresponding reduction kinetics of absorption band of **1** at 688 nm (left axis) together with potentials sweep profile (right axis).

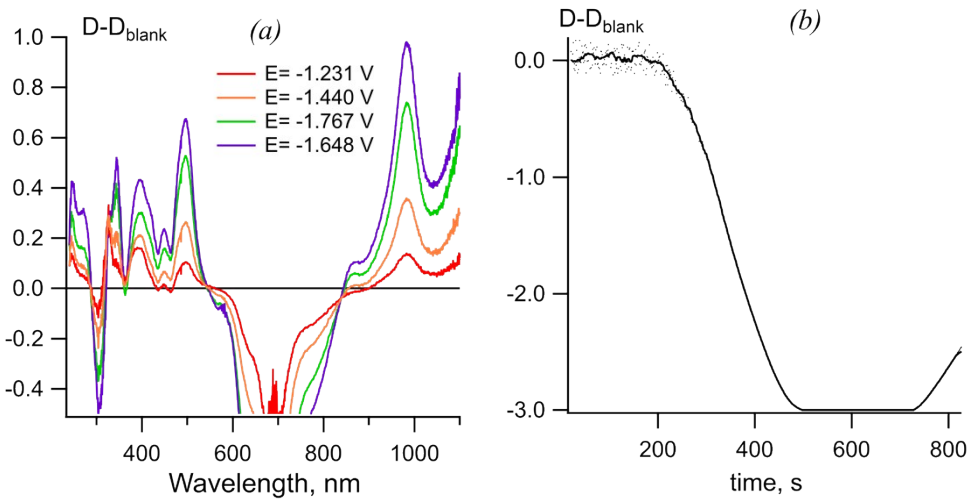

Figure S24. (*a*) Transient differential UV-Vis spectra recorded for concentrated (2 mM) THF solution of compound **1** upon electrochemical reduction; (*b*) the corresponding kinetics of the absorption band at 688 nm.

10. References

1 (*a*) S. Hadida, F. Van Goor, J. Zhou, V. Arumugam, J. McCartney, A. Hazlewood, C. Decker, P. Negulescu and P. D. J. Grootenhuis, *J. Med. Chem.*, 2014, **57**, 9776; (*b*) H. J. B. Biekart, H. B. Dessens, P. E. Verkade and B. M. Wepster, *Recueil*, 1952, **71**, 321.

2 G. M. Sheldrick, *SHELX-97, Programs for Crystal Structure Analysis (Release 97-2)*, University of Götingen: Germany, 1997.

3 G. M. Sheldrick, *Acta Crystallogr. C*, 2015, **71**, 3.

4 *SADABS, version 2008-1*, Bruker AXS: Madison, WI, USA, 2008.

5 (*a*) A. L. Spek, *PLATON, A Multipurpose Crystallographic Tool, Version 10M*, Utrecht University, The Netherlands, 2003; (*b*) A. L. Spek, *J. Appl. Crystallogr.*, 2003, **36**, 7.

6 C. F. Macrae, P. R. Edgington, P. McCabe, E. Pidcock, G. P. Shields, R. Taylor, M. Towler and J. van de Stree, *J. Appl. Crystallogr.*, 2006, **39**, 453.

7 S. Alvarez, *Dalton Trans.*, 2013, **42**, 8617.

8 (*a*) A. Yu. Makarov, I. Yu. Bagryanskaya, Yu. M. Volkova, M. M. Shakirov and A. V. Zibarev, *Eur. J. Inorg. Chem.*, 2018, **2018**, 1322; (*b*) A. Yu. Makarov, F. Blockhuys, I. Yu. Bagryanskaya, Yu. V. Gatilov, M. M. Shakirov and A. V. Zibarev, *Inorg. Chem.*, 2013, **52**, 3699; (*c*) M. Risto, A. Assoud, S. M. Winter, R. Oilunkaniemi, R. S. Laitinen and R. T. Oakley, *Inorg. Chem.*, 2008, **47**, 10100; (*d*) J. W. Bats, H. Fuess, K. L. Weber and H. W. Roesky, *Chem. Ber.*, 1983, **116**, 1751.

9 (*a*) A. D. Becke, *J. Chem. Phys*., 1993, **98**, 5648; (*b*) C. Lee, W. Yang and R. G. Parr, *Phys. Rev. B*, 1988, **37**, 785.

10 M. W. Schmidt, K. K. Baldridge, J. A. Boatz, S. T. Elbert, M. S. Gordon, J. H. Jensen, S. Koseki, N. Matsunaga, K. A. Nguyen, S. J. Su, T. L. Windus, M. Dupuis and J. A. Montgomery, *J. Comput. Chem.*, 1993, **14**, 1347.

11 F. Neese, *Wires Comput. Mol. Sci.*, 2018, **8**, e1327.

12 A. Dreuw and M. Head-Gordon, *Chem. Rev*., 2005, **105**, 4009.

13 S. Grimme and F. Neese, *J. Chem. Phys.*, 2007, **127**, 154116.

14 J. P. Perdew, K. Burke and M. Ernzerhof, *Phys. Rev. Lett.*, 1996, **77**, 3865.

15 F. Weigend and R. Ahlrichs, *Phys. Chem. Chem. Phys.*, 2005, **7**, 3297.

16 J. Tomasi, B. Mennucci and R. Cammi, *Chem. Rev.*, 2005, **105**, 2999.

17 A. V. Marenich, C. J. Cramer and D. G. Truhlar, *J. Phys. Chem. B*, 2009, **113**, 6378.

18 T. Petrenko and F. Neese, *J. Chem. Phys*., 2007, **127**, 164319.

19 M. de Jong, L. Seijo, A. Meijerink and F. T. Rabouw, *Phys. Chem. Chem. Phys*., 2015, **17**, 16959.

20 T. Petrenko and F. Neese, *J. Chem. Phys*., 2012, **137**, 23410.

21 L. Nadjo and J.-M. Savéant, *J. Electroanal. Chem.*, 1973, **48**, 113.

22 R. D. Duling, *J. Magn. Reson*., 1994, **104**, 105.